FLUORINE ADSORPTION AND DIFFUSION IN POLYCRYSTALLINE SILICA

DISSERTATION

Presented to the Graduate Council of the

University of North Texas in Partial

Fulfillment of the Requirements

For the Degree of

DOCTOR OF PHILOSOPHY

By

Jian-Yue Jin, B.S., M.S.

Denton, Texas

December, 1998

Jin, Jian-Yue, <u>Fluorine Adsorption and Diffusion in Polycrystalline Silica.</u>
Doctor of Philosophy (Physics), December, 1998, 80 pp., 31 illustrations, references, 72
titles.

The measurement of fluorine penetration into archeological flint artifacts using
Nuclear Reaction Analysis (NRA) has been reported to be a potential dating method.
However, the mechanism of how fluorine is incorporated into the flint surface, and finally
transported into the bulk is not well understood. This research focuses on the study of the
fluorine uptake phenomenon of flint mineral in aqueous fluoride solutions. Both
theoretical and experimental approaches have been carried out. In a theoretical approach,
a pipe-diffusion model was used to simulate the complicated fluorine transportation
problem in flint, in which several diffusion mechanisms may be involved.

A comprehensive experimental study was carried out. Scanning Electron
Microscopy (SEM), Transmission Electron Microscopy (TEM) and X-ray Fluorescence
Analysis (XRF) have been employed to study the microstructure and characteristics of the
sample materials. The NRA method was used to measure the fluorine and hydrogen
depth profiles in flint. Elastic Recoil Detection (ERD) was developed to monitor the
etching and dissolution of silica by the fluoride solution.

The fluorine uptake phenomenon was experimentally simulated by immersing
flint samples in sodium fluoride solutions with different fluoride concentrations and pH
values, at different temperatures, and for different times. The results suggest that fluorine

uptake is not a simple phenomenon, but rather a combination of several simultaneous

processes including surface adsorption and inward diffusion. Surface adsorption seems to

play an important role in developing the fluorine uptake profiles in flint. The surface

adsorption is found to increase as the pH value decreases, and as the fluoride

concentration increases in the solution. It is also found that the presence of Ca^{2+} in the

solution strongly enhances fluorine adsorption on the silica surface. The temperature of

the solution does not show a systematic relation with the adsorption results. Silica

etching is found to be insignificant in a neutral fluoride solution, but is observable in

basic and acidic solutions.

FLUORINE ADSORPTION AND DIFFUSION IN POLYCRYSTALLINE SILICA

DISSERTATION

Presented to the Graduate Council of the

University of North Texas in Partial

Fulfillment of the Requirements

For the Degree of

DOCTOR OF PHILOSOPHY

By

Jian-Yue Jin, B.S., M.S.

Denton, Texas

December, 1998

ACKNOWLEDGMENTS

I give my great appreciation to Dr. Samuel Matteson, my research advisor, for his expert advice, supportive discussions and continuous guidance in the course of my graduate study. I am especially grateful to Dr. Jerome L. Duggan for his warm support and encouragement in many ways. I thank Drs. Floyd D. McDaniel and Duncan L. Weathers, who always read and correct my writing carefully with many suggestions. My special appreciation also goes to Dr. Lon I. Morgan for his financial support when I was a visiting scholar here at the Ion Beam Modification and Analysis Laboratory (IMBAL), which finally led to my graduate study here.

I thank Dr. Oliver Chyan of the Chemistry Department for his helpful discussion and kindly loaning me the thermal bath. The helpful discussion with Dr. Richard Reidy of the Materials Science Department is acknowledged. I thank Mr. Yandon Chen for his help in making the TEM and SEM pictures. I would like to express my appreciation to Fiona Picton, Bryan Hughes, Dave Jedrejcic, Robert Greeson and other IBMAL friends for their technical assistance or correction of my writing.

Finally, I thank my wife Feng-Ming, my daughter Gracie, and my parents for their love, encouragement and patience.

The financial support from the Texas Advanced Research Program is gratefully acknowledged.

TABLE OF CONTENTS

v

LIST OF ILLUSTRATIONS

CHAPTER 1

INTRODUCTION

Surface adsorption and impurity diffusion are two very common and related

phenomena in nature. In addition to its fundamental interest to physicists, chemists, and

materials scientists, the study of these phenomena is of significant importance in many

fields such as geology, biology and environmental science, and is of great technological

and economic importance in industry.

The particular attention paid to the study of fluorine absorption and transportation

in polycrystalline silica was initially motivated by an attempt to develop a novel method

of dating archaeological stone artifacts. In 1975 Taylor first observed uptake of fluorine

into the surface of worked stone materials that had been buried in soil [TA75]. Walter et

al. in 1989 demonstrated that there was a strong correlation between the age of a flint

artifact and the depth of fluorine penetration into the surface [WA90, WA92]. This

suggests a potential method of dating archeological flints by measuring the fluorine depth

profile using Nuclear Reaction Analysis (NRA). However, the mechanism of how

fluorine is incorporated into the silica surface and finally penetrates into the bulk is not

well understood.

Walter et al. had studied solid state diffusion of fluorine in silica [WA92], which

is the principle constituent of flint. Samples were implanted with fluorine, followed by

high temperature annealing. An anomalous diffusion behavior was observed. At temperatures below 400°C, the implanted fluorine was virtually immovable. At temperatures between 400°C and 500°C, there was a small shift of the peak toward greater depth and a noticeable fluorine loss, while at temperatures above 500°C, the fluorine peak rapidly disappeared. Similar diffusion behavior was also found for fluorine diffusion in silicon [SZ94, JE92, MA92, TS79], and chlorine diffusion in silicon [DA95]. These results argue against the role of solid state diffusion in fluorine transportation in flint since the reported behavior of fluorine in fused silica is markedly different from that observed in mineral samples.

It has been speculated that the source of fluorine uptake is ground water. This contention has been partially confirmed by Walter's work [WA90], in which he observed penetration profiles of fluorine in flint samples by placing them in fluoride solutions of various concentrations. However, no time-dependent study has been reported, and the role of the fluorine uptake in developing the penetrated fluorine profiles is not clear.

Fluorine uptake in silica from fluoride solutions is similar in some features to the process of silica etching by hydrofluoric acid, which has been extensively studied and has important applications in wafer cleaning and pattern delineation in integrated circuit (IC) manufacturing [JU71, LI87, OS96]. In general, the kinetics of silica etching is characterized by the following steps: (i) fluorine adsorption onto the silica surface, (ii) surface reaction, (iii) dissolution of surface species [OS96]. However, in spite of the numerous publications dealing with various aspects of aqueous chemical processes, the

physicochemical details of the SiO_2-HF-H_2O reaction are still not totally understood. The rate of the etching process still depends on an empirical approach.

The fluorine uptake phenomenon is, however, very different from silica etching processes in many aspects, such as the different fluorine concentrations and pH values of the solution. Another particular difference is the unique microstructure of flint. The typical microstructure of flint or chert is reported to be granular microquartz cemented with amorphous silica [GR94, SH72]. The amorphous phase of silica could be bundles of nano-size fiber quartz [GR94, WA90, CH81], or opal like silica [SH72], or any other amorphous phase of silica, depending on the type of flint. There is a considerable amount of water in the amorphous silica structure, which usually occupies the interstitial spaces between the quartz fiber or silica spheres. Alternatively, polycrystalline silica with small-void networks containing water might represent the major structure of various forms of flint.

Based on the microstructure of the flint mineral and some experimental results, the fluorine uptake phenomenon is conceived of as the combination of the following possible simultaneous processes: (i) Fluorine adsorption on the flint surface; (ii) Fluorine ion diffusion along the void network in the liquid phase and final adsorption by the surface (wall) of the voids; (iii) Diffusion of adsorbed fluorine ions along the surface of the grains, or amorphous silica spheres analogous to so called grain boundary diffusion; (iv) Diffusion of adsorbed fluorine into the bulk, in a manner reminiscent of solid state diffusion; (v) Gradual dissolution of surface species.

Unfortunately, due to the rough surface and the void structure of the flint sample, the surface is not clearly delineated. In this study the flint surface is defined as the solid–liquid interface for which the liquid-phase ion diffusion rate is not significantly slowed down by the limited size of the reticulated network available to the liquid phase. More clearly, the surface area includes large open volumes (voids) into which the diffusion of fluorine ions proceeds at a rate similar to that in the solution. Other small open voids are considered to be diffusion channels because the ion diffusion rate in these small voids is substantially slower than that in the solution.

This dissertation focuses on the study of the fluorine uptake phenomenon in the flint mineral from the aqueous solution, which covers all five processes aforementioned. However, surface adsorption has been paid special attention because it is found that it seems to play the central role in developing the fluorine profiles.

The fluorine-uptake phenomenon was experimentally simulated by immersing flint samples in a sodium fluoride (NaF) solution under different conditions, for example, with different fluorine concentrations and pH values of the solution, at different temperatures for different times and so on. Resonance Nuclear Reaction Analysis (NRA) was used to measure the fluorine surface concentration and the fluorine depth profile in the materials. The $^{19}F(p, \alpha\gamma)^{16}O$ reaction at a proton energy of 872 keV was used. This is a well-understood reaction with a cross section of about 540 mb and a resonance width of about 4.5 keV [MA77]. The reaction is widely used in fluorine depth profiling. Other material characterization methods, such as Scanning Electron Microscopy (SEM),

Transmission Electron Microscopy (TEM), and X-ray fluorescence spectrometry (XRF) were employed to study the microstructure and characteristics of the flint material. Another NRA method, using the $^1H(^{19}F, \alpha\gamma)^{16}O$ reaction at a fluorine energy of 6.42 MeV [BA77, CL78], was utilized to measure the hydrogen profiles. Elastic Recoil Detection (ERD) was employed to measure the oxygen concentration [BA95, EC76, DO79], and thereby monitoring the etching of silica by the fluoride solutions.

This dissertation is divided into six chapters. Chapter 2 describes the basic theory of surface adsorption and solid state diffusion. Chapter 3 discusses theoretical simulations of complex grain boundary diffusion via a pipe diffusion model. Chapter 4 deals with the development of the experimental methods. In Chapter 5, experimental results and discussion are given. And, finally, Chapter 6 summarizes and concludes the dissertation.

CHAPTER 2

THEORY

In this chapter the basic theory related to this dissertation is reviewed. Namely, the theories of surface adsorption and solid state diffusion are outlined. Corresponding to the unique poly-crystalline and void microstructure of flint, a pipe diffusion model is also examined.

2.1 Surface Adsorption

2.1.1 Solid Surface and Surface Adsorption

The surface of a solid is the boundary layer of lattice units (atomic, ionic or molecular) that terminates the lattice. The particles at surfaces suffer from an imbalance of chemical forces. This imbalance may be expressed in terms of surface energy. Thus, a finely dispersed solid phase tends to lower its surface energy, either by reducing its surface area (surface distortions), or by adsorbing molecules and ions from adjacent phases.

Surface adsorption is defined as the bonding of particles at the surface which differ from the constituents of the lattice and do not penetrate into the lattice [RO97, MO90]. There are generally two types of adsorption: (i) physical adsorption, and (ii)

chemical adsorption or chemisorption. Physical adsorption usually happens when the attractive forces between the solid (adsorbent) and the adsorbed species (adsorbate) are weak, and hydrogen bonding and Van de Waals bonds are often responsible. It is usually a reversible process, and the adsorption often takes place rapidly. Chemisorption, in contrast, is usually the result of strong attractive forces of primary valence bonds between the adsorbent and adsorbate. It is an irreversible process, and often accompanies dissociation. In fact, chemisorption is a chemical reactive process.

2.1.2 Adsorption Kinetics

Adsorption kinetics is usually represented by the adsorption rate R_{ads} [RO97, MO90, VO83], which is determined by two factors. These are F, the flux of incident molecules arriving at the surface, and S, the sticking probability. Therefore, the adsorption rate is given by

$$R_{ads} = S \cdot F.$$ (2.1)

The sticking probability S can, in general, be expressed as

$$S = f(\theta) \cdot \exp(-E_a/RT),$$ (2.2)

where θ is the existing concentration of adsorbed species on the surface, f is a function of θ, which is usually dependent on the percentage of sites not being occupied by the adsorbate, and E_a is the activation energy barrier to adsorption. The flux, F, is the product of adsorbate density and its average velocity toward the surface. In the case of adsorption in a gas phase, it is given by

$$F = P/(2\pi mkT)^{1/2} , \tag{2.3}$$

where P is the gas pressure, m is the mass of the molecule, k is Boltzmann's constant, and T is the absolute temperature.

In the case of adsorption from a solution, equation (2.3) is no longer valid, and no explicit formulation of adsorbate flux in solutions were found in the literature. However, in general, the flux can be expressed simply as

$$F = CD_{sol}(T) , \tag{2.4}$$

where C is the concentration of adsorbate in the solution, and D_{sol} is the diffusion coefficient in the diffusion layer in the solid-liquid interface. A more detailed discussion of adsorption from solutions is given in section 2.1.4. Nevertheless, the diffusion coefficient D_{sol} should be dependent on several parameters such as adsorbate species, the solid-liquid interface and temperature.

Combining the aforementioned equations for S and F yields the following expressions for the adsorption rate; for gas adsorption, it is

$$R = \frac{f(\theta)P}{\sqrt{2\pi mkT}}\exp(-E_a/kT) , \tag{2.5}$$

and for adsorption from a solution, it is

$$R = f(\theta)CD_{sol}(T)\exp(-E_a/kT) . \tag{2.6}$$

Equations (2.5) and (2.6) give the expression of adsorption kinetics in terms of adsorption rate. However, it is often more practical to express the kinetics in the form of

the variation of the amount of adsorption with time. This is approached by using the Elovich equation [HA64, HI81], the simplest form of which is

$$\frac{dq}{dt} = a\exp(-bq),$$ (2.7)

where q is the amount of adsorbate taken up in time t, a is a constant related to the initial rate of reaction, and b is a constant related to the activation energy for adsorption.

Equation (2.7) can be rearranged as

$$(dq)\exp(bq) = a(dt).$$ (2.8)

Integrating Equation (2.8) with the boundary condition $q = 0$ at $t = 0$ gives

$$q = b^{-1}\ln(1 + t/k),$$ (2.9)

where $k = (ab)^{-1}$. However, in analysis adsorption kinetics, a pre-Elovichian stage is often postulated, leading to the boundary condition $q = q_0 \neq 0$ at $t = 0$, giving the integrated form

$$q = b^{-1}\ln(1 + t/k) + q_0,$$ (2.10)

where $k = (ab)^{-1}\exp(bq_0)$.

Equations (2.9) and (2.10) are also called the Elovich equation and can be used to fit the experimental kinetics data. It appears that other processes related to the surface reaction will also obey the Elovich equation. For example, the oxide formation model of Ritchie [RI69] follows the same Elovich equation, and it also has been applied for metal oxidation as well as oxidation of semiconductors by Matteson et al. [MA85].

2.1.3 Equilibrium Condition--Langmuir Isotherm

The adsorption process is always followed by desorption, or adsorbate diffusion into the bulk of the underlying solid, or by a dissociation reaction, or all of these processes. Considering the simplest case, in which the adsorption process is followed only by desorption, equilibrium is reached when the adsorption rate is equal to the desorption rate. The isothermal relation at the equilibrium condition is usually used to describe the adsorption properties [RO97, VO83].

The rate of desorption can be expressed as

$$R_{des} = f_1(\theta) \exp(-E_a^{des} / kT),$$ (2.11)

where $f_1(\theta)$ is another function of θ which may vary with different adsorbate/adsorbent systems. When equilibrium is reached, it can be shown from equation (2.5), (2.6) and (2.11) that in the case of gas adsorption,

$$\frac{Pf(\theta)}{f_1(\theta)} = \frac{\sqrt{2\pi mkT}}{\exp[-(E_a^{ads} - E_a^{des})/kT]} = \alpha(T),$$ (2.12)

or in the case of adsorption from a solution,

$$\frac{Cf(\theta)}{f_1(\theta)} = \alpha_1(T).$$ (2.13)

The Langmuir isotherm is one of the several types of isotherms that is used to describe the behavior of gas adsorption. It is derived with the assumption that $f(\theta)$ is proportional to the percentage of sites not being occupied, while $f_1(\theta)$ is proportional to the percentage of sites being occupied. Therefore, it has

$$f(\theta) = \beta(1 - \theta) \qquad \text{and} \qquad f_1(\theta) = \beta_1\theta, \tag{2.14}$$

where β and β_1 are constants that depend on the adsorbate/adsorbent system.

Substituting equation (2.14) into (2.12), it gives

$$\frac{P(1-\theta)}{\theta} = \frac{\beta_1}{\beta}\alpha(T), \tag{2.15}$$

or

$$\theta = \frac{b(T)P}{1+b(T)P}, \tag{2.16}$$

where $b(T) = \dfrac{\beta}{\beta_1\alpha(T)}$ is a parameter only depended on temperature T.

Equation (2.16) is the famous Langmuir isotherm [LA18, VO83]. It is based on the assumption that adsorption is limited to only a single molecular layer. However, in many situations, a surface is capable of adsorbing several layers of foreign molecules. Other types of isotherms such as the Brunauer-Emmett-Teller (BET) [BR38] isotherm have been proposed to describe this adsorption behavior. In the case of adsorption from a solution, since more than one species (solution and solvent, or positive and negative ions) are competing to be adsorbed in the available sites, the adsorption isotherm becomes much more complicated.

2.1.4 Anion Adsorption at the Aqueous-Solid Interface

Because this dissertation focuses on the study of fluorine uptake from the aqueous solution, knowledge of anion adsorption at the aqueous-solid interface is particularly important. Ion adsorption at the aqueous-solid interface is different from other surface

adsorption phenomena because of the following two facts: (i) The aqueous-solid interface is usually charged because the solid surface itself may have a surface potential, and the potential-determining ions (OH^-, H^+, cations, anions) at the surface coordination complex layer are usually imbalanced; (ii) The ions in the solution exist as charged particles and are free to move.

The model that describes the charged phenomenon at the liquid-solid interface has undergone several evolutions, as illustrated in Fig.2.1 [JE97, AD97]. The first model assumed a fixed (rigid) electrical double layer and was proposed by Helmholtz in 1879.
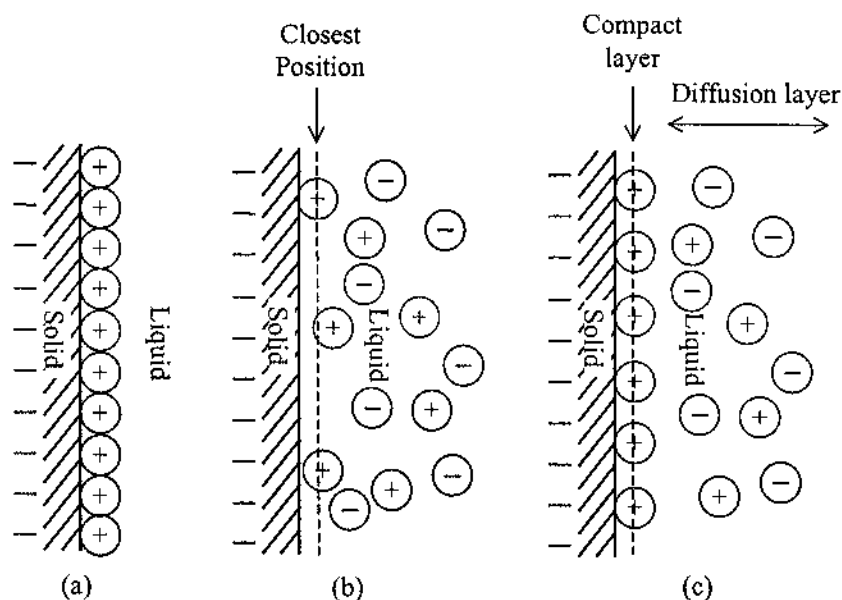
Fig. 2.1. Evolution of the charged surface double layer models. (a) The Helmholtz fixed (rigid) double layer; (b) the Gouy-Chapman diffuse double layer; (c) the Stern double layer, being a combination of the Helmholtz and Gouy-Chapman concepts.

According to this model, a positively-charged surface attracts negative ions from the solution and vice versa. Between 1910 and 1913, Gouy and Chapman modified this idea and proposed a diffuse double layer model. According to this model, the attracted ions should extend some distance from the solid surface and follow a Boltzmann distribution in position.

The two distinct models were combined into a new one by Stern in 1924. In this new model, it is recognized that the electrified solid-liquid interface comprises both a fixed Helmholtz layer (compact layer) and a diffuse layer. However, the Stern model still does not reflect the real picture of the phenomenon at the solid-liquid interface. Specially, it neglects the effects of adsorbed solvent molecules at the interface. A modified model, that has been generally accepted, is illustrated in Fig. 2.2 [JE97, AD97].

In this modified model, the fixed Stern layer (or compact layer) is considered to be the surface coordination complexes, and is divided into an inner-sphere complex layer and an outer-sphere complex layer. Ions bonded in the inner sphere complex have different chemical properties from ions bonded in the outer-sphere complex. Nevertheless, the final surface potential is determined by the combination of the charge distribution in the original solid surface and the potential-determining ion distribution in this compact layer (both inner and outer layers). Ion adsorption is very dependent on this surface potential [HI81].
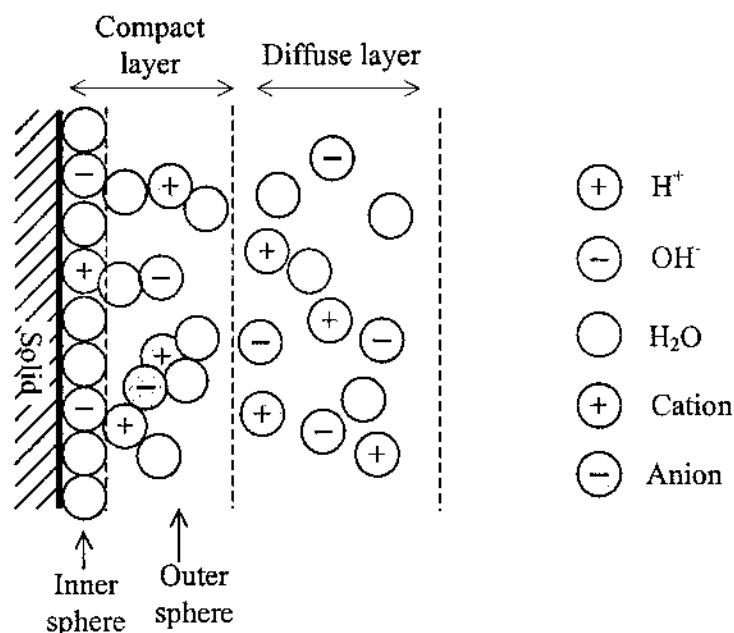
Fig. 2.2. A generally accepted electrical double layer model in
the aqueous-solid interface

The pH value of the solution usually changes the final surface potential in the
aqueous-solid interface. The lower the pH value, the greater the H^+ concentration in the
solution; consequently, more positive H^+ ions are included in the compact layer, and the
surface potential tends to be more positive. Therefore, usually, a lower pH value
increases the anion surface adsorption while it decreases cation adsorption and vice versa.
There is a critical point of pH value at which the surface charge becomes balanced. This
point of pH value is defined as the point of zero charge (pzc), and is used to characterize
the charging property of an aqueous-solid interface [JA81, OS96]. The pzc of a silica-
aqueous interface is reported to be between 2.5 to 3 [OS96, DO94]. Therefore, the silica
surface is more likely to adsorb a cation (like Ca^{2+}) rather than an anion (like F^-) in a
neutral solution.

2.2 Solid State Diffusion

2.2.1 Random Walks and Fick's Laws

At the most basic level, diffusion is a consequence of a random walk in the presence of a concentration gradient [MA90, BO88]. If the frequency of the jumps between sites is independent of the site, then there is a net flux of atoms or molecules from regions of higher concentration to regions of lower concentration. This is formally expressed as Fick's first Law:

$$\vec{J}(\vec{x}, t) = -D\nabla C(\vec{x}, t),$$
(2.17)

where $\vec{J}$ is the flux, D is the diffusion coefficient and C is the concentration. Combining the continuity equation

$$\frac{\partial C}{\partial t} = -\nabla \cdot \vec{J}$$
(2.18)

with Fick's first Law, and assuming D is independent of the position x, Fick's Second Law is obtained as

$$\frac{\partial C}{\partial t} = D\nabla^2 C.$$
(2.19)

In the case of one dimensional diffusion, Fick's Second Law becomes

$$\frac{\partial C}{\partial t} = D\frac{\partial^2 C}{\partial x^2}.$$
(2.20)

The diffusion constant D is dependent on the jump frequency and distance. If the atom encounters an energy barrier of $\Delta E = E_a$ at each jump, it can be shown that [MA90]

$$D = D_0 \exp(-E_a/kT).$$
(2.21)

The solution of the diffusion equation is dependent on the boundary conditions. Two boundary conditions are commonly used in experiments, for which the diffusion equation is analytically solvable. They are:

1) Surface concentration C_S is kept constant. The solution is thus

$$C(x,t) = C_s \, \text{erfc}\left(\frac{x}{\sqrt{4Dt}}\right).$$

$$(2.22)$$

2) The total diffusing amount Q is constant. The solution has the form of a Gaussian function,

$$C(x,t) = \frac{Q}{\sqrt{\pi Dt}} \exp\left(-\frac{x^2}{4Dt}\right).$$

$$(2.23)$$

Other experimental conditions frequently prevail in the laboratory for which no analytic solution exists.

2.2.2 Diffusion in Poly-Crystalline Material--Pipe Diffusion Model

The above solutions are only valid for diffusion in homogeneous media. However, the flint samples used in this study have mixed microstructures of poly-crystalline silica and amorphous silica with a reticulated void network. Diffusion rates in different structures, such as in the crystal grains or in the amorphous bulk, and along the grain boundaries or along the void network, are all very different. Therefore, the diffusion phenomenon in flint samples is very complicated. In this section, a pipe diffusion model is examined. This model was proposed to solve the complicated grain

boundary diffusion problem, which is similar in many features to the diffusion

phenomenon in flint.

Diffusion along the grain boundary has been under extensive study both

experimentally and

theoretically in the past

decades due to its

importance in materials

science [KA89, CH96,

PO96]. Fisher started the

pioneering theoretical

approach by suggesting a

Fig. 2.3. The pipe diffusion model, in which the medium is considered as a semi-infinite bicrystal with boundary width of 2a.

pipe diffusion model [FI50]. In this model, a semi-infinite 2-dimensional bicrystal

medium was considered (see Fig. 2.3). Then the concentration $C(x, y, t)$ in the medium

must satisfy the following equations [FI50]:

$$\frac{\partial C}{\partial t} = D\left(\frac{\partial^2 C}{\partial x^2} + \frac{\partial^2 C}{\partial y^2}\right) \qquad \text{when} \qquad x > a, \qquad (2.24a)$$

$$\frac{\partial C}{\partial t} = D_b \frac{\partial^2 C}{\partial y^2} + \frac{D}{a}\frac{\partial C}{\partial x} \qquad \text{when} \qquad x = \pm a, \qquad (2.24b)$$

where D and D_b are the diffusion coefficients in the bulk and the grain boundary

respectively, and a is the half width of the grain boundary. Fisher also gave the following

simplified approximate solution for the equations:

$$C(x,y,t) = \exp\left(-\frac{\sqrt{2}y}{(aD_b/D)^{1/2}(\pi Dt)^{1/4}}\right) \cdot \text{erfc}\left(\frac{x}{2\sqrt{Dt}}\right). \tag{2.25}$$

However, equation (2.25) turned out to be over simplified, and it is not totally correct.

Based on the same pipe diffusion model, Whipple derived an exact solution for this problem by means of Fourier and Laplace transforms [WH54]. His solution was given as

$$C = \text{erfc}\,\eta + \frac{\eta}{2\sqrt{\pi}}\int_1^\Omega \frac{d\sigma}{\sigma^{3/2}}\exp\left(-\frac{\eta^2}{4\sigma}\right)\text{erfc}\left(\frac{1}{2}\sqrt{\frac{\Omega-1}{\Omega-\sigma}}\left(\xi+\frac{\alpha-1}{\beta}\right)\right), \tag{2.26}$$

where

$$\xi = \frac{x-a}{\sqrt{Dt}}, \qquad \eta = \frac{y}{\sqrt{Dt}}, \qquad \Omega = \frac{D_b}{D} \quad \text{and} \quad \beta = \left(\frac{D_b}{D}-1\right)\frac{a}{\sqrt{Dt}} \approx \frac{\Omega a}{\sqrt{Dt}}.$$

However, due to its integral form, this solution is by no means easy to apply to realistic experimental situations.

Later on, Le Claire and Suzuoka analyzed Whipple's solution using numerical calculations of the integral form [CL63, SU64]. They concluded that under the conditions of approximately

$$\eta/\sqrt{\beta} > 2 \qquad \text{and} \qquad \beta > 10, \tag{2.27}$$

the average solute concentration distribution could be approximately expressed as the following:

$$\overline{C} \propto \exp\left(-\left(\eta/\beta^{1/2}\right)^{6/5}\right). \tag{2.28}$$

Referred to as the exponential rule, equation (2.28) was widely used in the sectioning experiments to determine grain boundary diffusion coefficients D_b [PO96, CH96, EV96, KA89]. However, there are limitations in this result [CH96]. It is only valid under the condition of relation (2.27). In terms of depth y, the first part of relation (2.27) becomes

$$y > 2\sqrt{Dt\beta} = 2\sqrt{\Omega a}\left(Dt\right)^{1/4}.$$

$$(2.29)$$

Therefore, equation (2.28) is not valid in the near surface region, where the experimental results are usually available. Moreover, this result was derived from the semi-infinite bicrystal structure. The effects of complicated polycrystalline structure and grain size are ignored. In the next chapter, an alternative approach, namely, the finite difference method, will be presented to solve a similar problem.

CHAPTER 3

A NUMERICAL STUDY OF THE PIPE DIFFUSION MODEL

The exponential rule mentioned in the last chapter is not valid in the near surface region, where depth profiling data by the NRA method are usually available. Moreover, this result was derived from the semi-infinite bi-crystal structure. It ignores the complication of polycrystalline structure. In this chapter, an alternative approach, namely, the finite difference method, is used to simulate the grain boundary diffusion problem. This method should also be applicable to similar diffusion problems in flint samples.

3.1. The Finite Difference Method

The finite difference method has been used to solve the diffusion equations for polycrystalline material [JI97b]. For simplification, it is assumed that the polycrystalline medium is a two-dimensional structure with equal-sized rectangular grains (see Fig. 3.1a). The "grains" are topologically equivalent to any non-permeable microstructure, e.g., as in amorphous spheres. Moreover, by considering the solution to this non-realistic model, one can obtain an understanding of the nature of the diffusion process and the mathematical form of the expected distribution. Each grain has width of $2G$ and length of L_y. The boundary between two grains has a width of $2a$. A constant concentration C_0 is kept at the surface $y = 0$ during the diffusion process. It is also assumed that either

L_y is large enough or the diffusion time is short enough that the foreign species diffuse only into the first grain layer. Due to symmetry, the concentration distribution in half a grain (see Fig. 3.1b) may represent the distribution in the whole infinite medium.
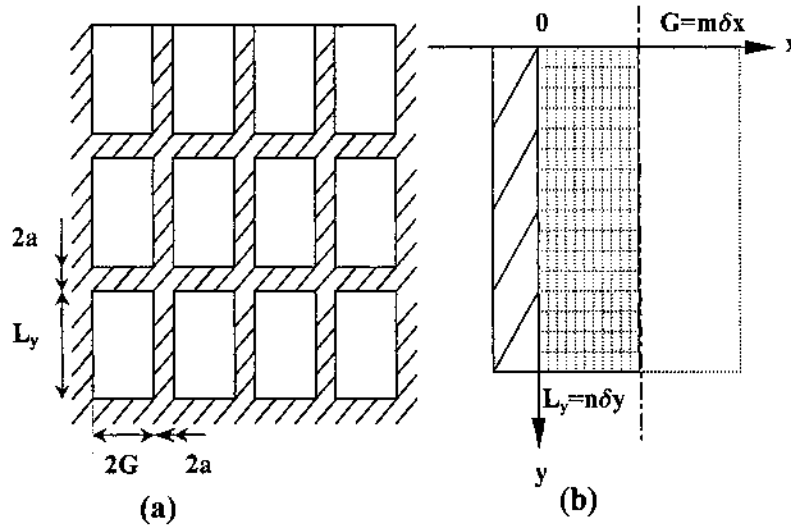
Fig. 3.1, The Pipe diffusion model in a 2-D poly-crystalline structure with $2G \times L_y$ grain and grain boundary width of $2a$.

The half grain in Fig. 3.1b is divided into $m \times n$ small units. Then, according to the finite difference method [GE70], the pipe diffusion equation (2.24) can be expressed as follows:

$$\delta C_{0,j} = \left(\Omega \frac{C_{0,j+1} + C_{0,j-1} - 2C_{0,j}}{\delta y^2} + \frac{1}{a} \frac{C_{1,j} - C_{0,j}}{\delta x} \right) \delta t , \tag{3.1a}$$

$$\delta C_{i,j} = \left(\frac{C_{i,j+1} + C_{i,j-1} - 2C_{i,j}}{\delta y^2} + \frac{C_{i+1,j} + C_{i-1,j} - 2C_{i,j}}{\delta x^2} \right) \delta t , \tag{3.1b}$$

$$C_{i,j}(t + \Delta t) = C_{i,j}(t) + \delta C_{i,j}, \tag{3.1c}$$

where $\delta t = D\Delta t$.

The initial condition is

$$C_{i,0}(t = 0) = 1, \qquad C_{i,j}(t = 0) = 0, \tag{3.2}$$

and the boundary condition is

$$C_{i,0}(t) = 1, \quad C_{i,n+1}(t) = 0, \quad C_{m+1,j}(t) = C_{m-1,j}(t). \tag{3.3}$$

The average concentration at depth $j\delta y$ is

$$\overline{C_j} = \frac{a}{a+G}C_{0,j} + \frac{\delta x}{a+G}\sum_{i=1}^{m} C_{i,j}. \tag{3.4}$$

With the above algorithm, the solute concentration at any position and at any time can be calculated.

3. 2. Results

$C_{i,j}$, the concentration at each unit, and $\overline{C_j}$, the average concentration as a function of depth, were calculated for the following conditions: $a = 5$ Å; $\Omega = 100, 1000, 10000,$ 100000; $G = 400, 800, 1600, 3200$ Å; and at different times. Fig. 3.2 shows the typical calculated 2-D concentration profiles. One sees the general evolution of the solute profile as time increases.

Fig. 3.3 shows the simulated concentration distribution along the grain boundary for different diffusion times and under different conditions. It shows that the concentration distribution along the boundary follows the exponential rule very well in almost all time and depth regimes. And the profiles can be fitted to:

$$C_b(y,t)/C_0 = \exp\left(-(y/b)^\gamma\right). \tag{3.5}$$

where b is a fitting parameter varying with time, and γ is a constant, which may vary a little (from 1.0 to 1.5) in different time regimes. In most time regimes, γ is $1.1 \sim 1.2$ (When diffusion time is very short, γ tends to be large; when the time is very long, γ tends to be small). This result agrees with Le Claire's very well [CL63].
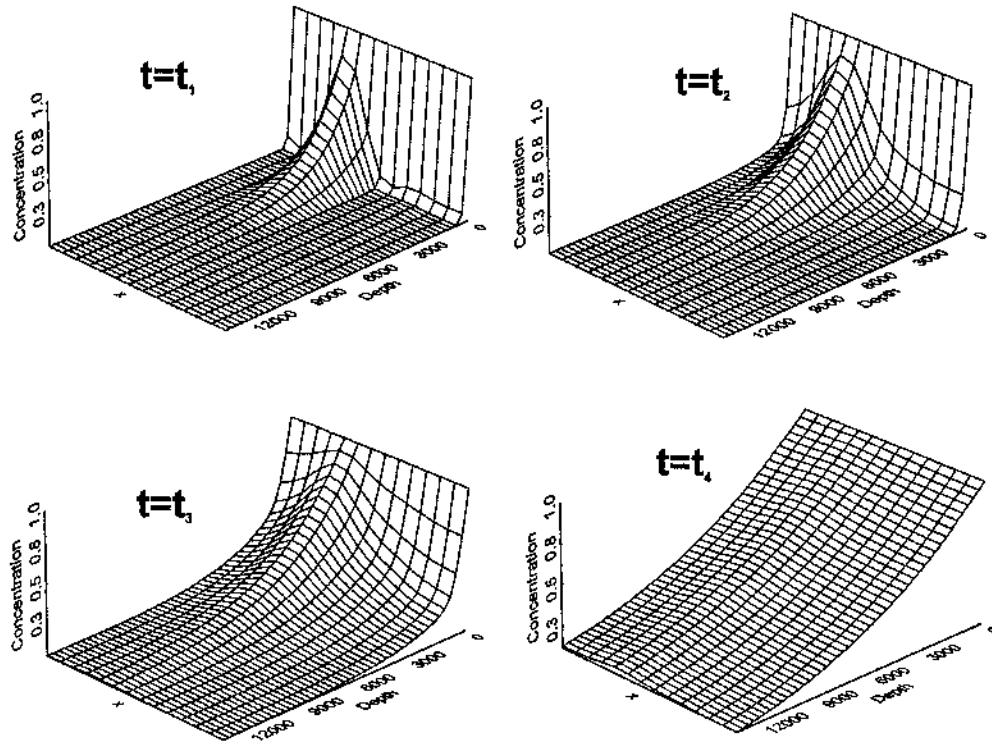
Fig. 3.2. Numerical calculated 2-D concentration distribution with G=800 Å, Ω=1000 after different times of diffusion, $t_1 < t_2 < t_3 < t_4$.
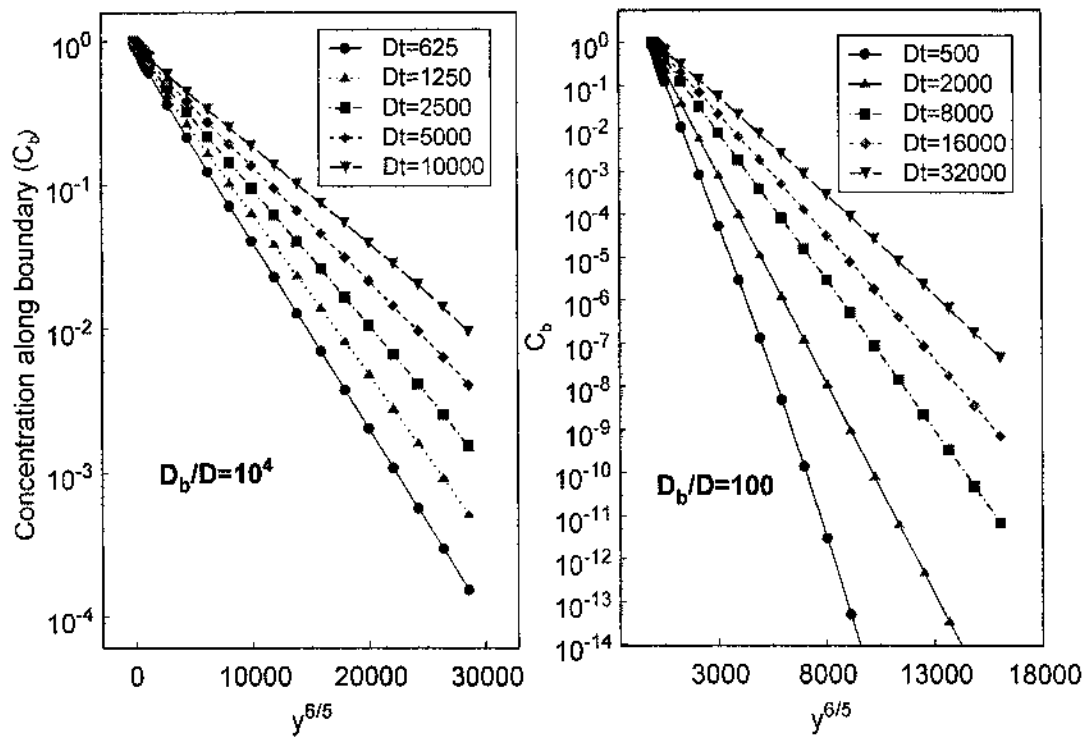
Fig. 3.3, Calculated solute concentration distribution along the grain boundary for different times and at different conditions.
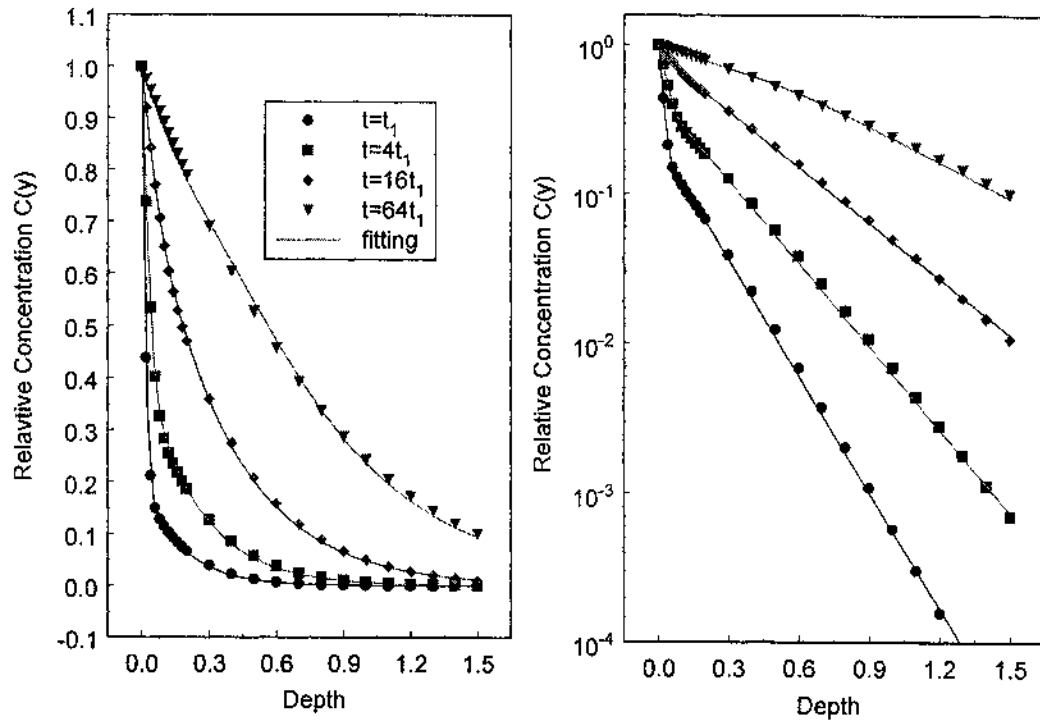
Fig. 3.4, Numerically calculated average concentration distribution with $G = 800$ Å, $\Omega = 1000$ after different times of diffusion. The left and the right figures are the same except that the y-axis of the left one is in linear scale, while the right one is in exponential scale.

The experimentally measured depth profile is usually the average concentration distribution. Fig. 3.4 shows a typical calculated result of the average depth profiles in different time regimes. The data can be fitted quite well as the combination of two functions:

$$\overline{C}(y,t)/C_0 = (1-k)\text{erfc}(y/b_1) + k\exp\left(-\left(y/b_2\right)^{1.15}\right), \tag{3.6}$$

where k, b_1, and b_2 are fitting parameters, which are dependent on the time t, and the diffusion parameters Ω and G. The complementary error function represents the bulk diffusion from the surface into the grain. The 1.15 power exponential function represents the diffusion along the grain boundary and from the boundary into the grains. The power index of 1.15 in equation (3.6) may not always be the best value to fit the profiles (generally varies from 1.10 to 1.20). However, to be consistent, equation (3.6) with the same power index of 1.15 was used to fit all the profiles with different conditions. As a matter of fact, from the experimental viewpoint, the difference between the fits for 1.15 power, 1.20 power, or even 1.00 power is negligible. All these power exponential terms are referred simply as the exponential term in the rest of the chapter.

By fitting the profiles for different conditions with equation (3.6), the relations of the parameters k, b_1, and b_2, to time t, and the parameters Ω and G can be obtained from the numerical data. They are shown in Fig. 3.5, Fig. 3.6 and Fig. 3.7, respectively. It is found that they are fitted quite well with the following empirical expressions,

$$k = \frac{a}{G} + \frac{\sqrt{Dt}}{G}(1 + O[1/\beta]), \tag{3.7a}$$

$$b_1 = 2\sqrt{Dt}(1 + O[1/\beta]), \tag{3.7b}$$

$$b_2 = \sqrt{\Omega a}(Dt)^{1/4}(1 + \varepsilon)(1 + O[1/\beta]), \tag{3.7c}$$

where $O[1/\beta]$ is a first order small function of variable $1/\beta$, and ε is a coefficient related to Ω that can be approximately expressed as $\varepsilon = \dfrac{\ln \Omega}{40}$.
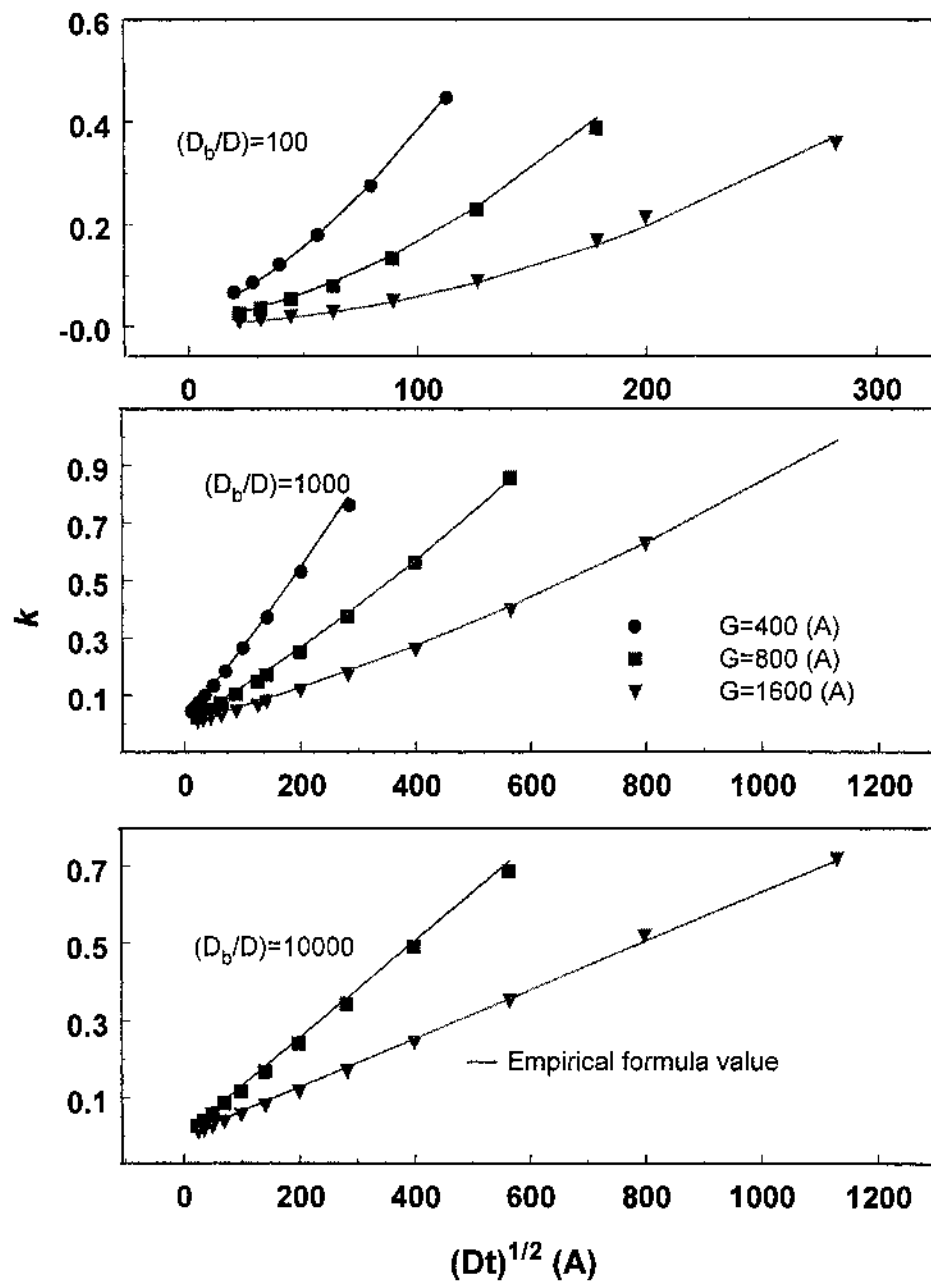
Fig. 3.5, Relation of the parameter k to time t, and the parameters Ω and G.
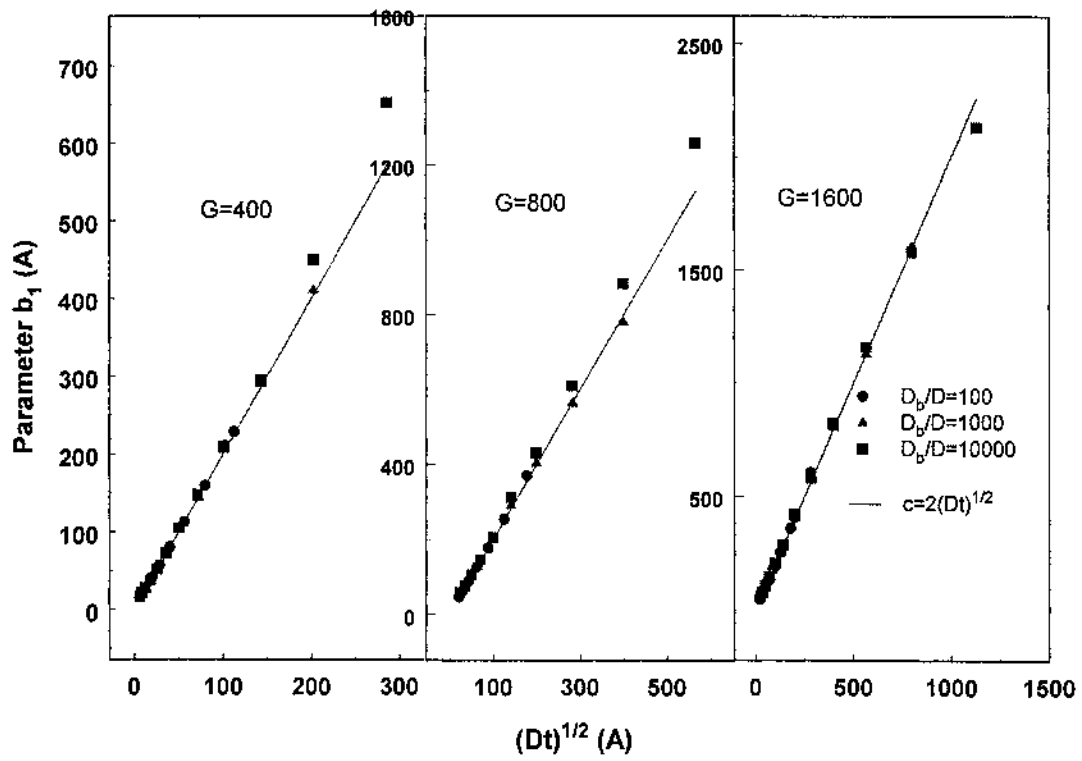
Fig. 3.6, Relation of the parameter b_1 to time t, and the parameters Ω and G.
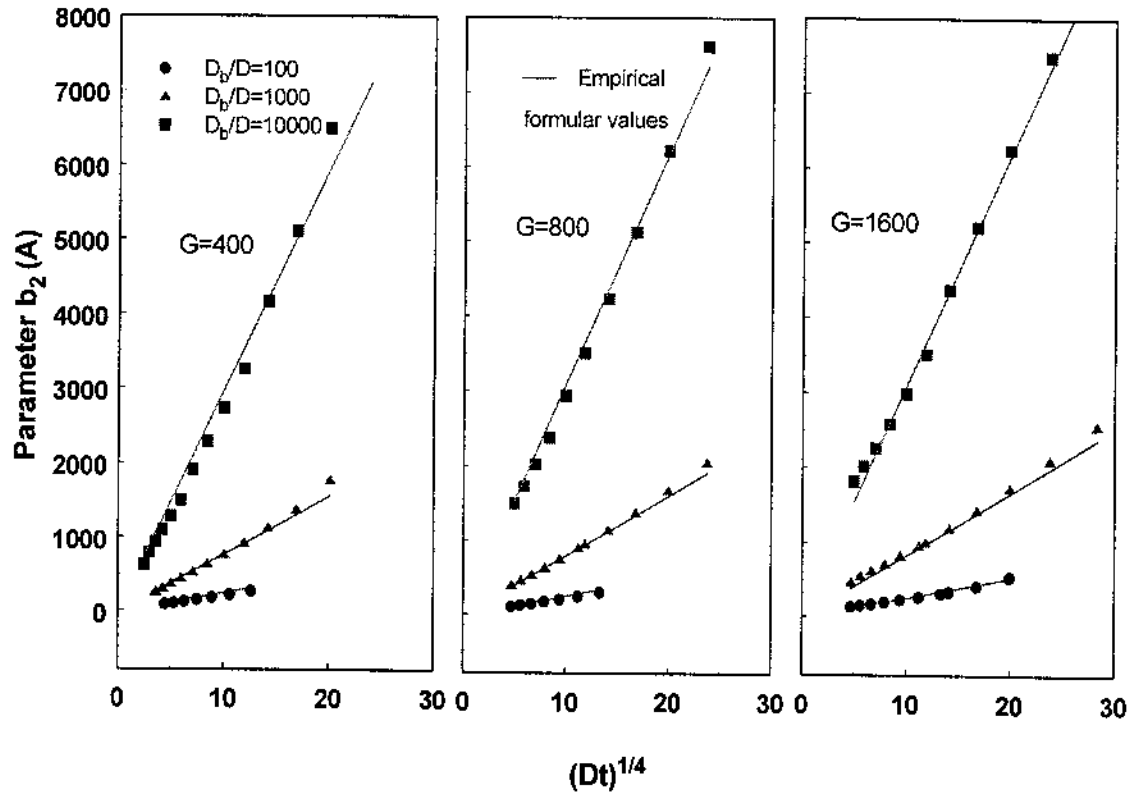
Fig. 3.7, Relation of the parameter b_2 to time t, and the parameters Ω

3.3 Discussion and Summary

Equation (3.6) can be physically interpreted as the result of two combined diffusions. The first term, the complimentary error function, corresponds to the pure bulk diffusion from the surface into the grains. The second term, the 1.15 power exponential function, corresponds to diffusion along the grain boundary and from the boundary into the grains in the x direction. The parameter k reflects the portion of the area of the grain being diffused from the boundary in the x direction. The increase in k with the diffusion time indicates that the portion subject to diffusion along grain boundaries and from grain boundaries into the grains is increasing with time, while the portion subject to pure bulk diffusion is decreasing with the time.

Parameters b_1 and b_2 reflect the depths of the two diffusion terms. It is of interest to notice that b_1 and b_2 are proportional to $(Dt)^{1/2}$ and $(Dt)^{1/4}$, respectively. Considering ϑ as the ratio of these two characteristic depths, it can be shown that

$$\vartheta = \frac{\sqrt{Dt}}{(1+\varepsilon)\sqrt{\Omega a}\,(Dt)^{1/4}} = \frac{(Dt)^{1/4}}{(1+\varepsilon)\sqrt{\Omega a}} = \frac{1}{(1+\varepsilon)\beta^{1/2}}.$$

(3.8)

When $\vartheta > 1$, or $\beta < 1/(1+\varepsilon)^2$, or $\sqrt{Dt} > \Omega a(1+\varepsilon)^2$, the depth of the pure bulk diffusion term begins to catch up with that of the grain boundary diffusion term. Therefore, the diffusion process could be divided into the following three regimes according to different ϑ or β values:

1) When $\vartheta \ll 1$, or $\sqrt{Dt} \ll \Omega a(1+\varepsilon)^2$, diffusion in polycrystalline material is the combination of the complimentary error function term and a power exponential function term, as described by equation (3.6).

2) When $\vartheta \sim 1$, or $\sqrt{Dt} \sim \Omega a(1+\varepsilon)^2$, the complimentary error function and the power exponential function have similar depths. It was found that in this region the combination of the two could be approximately expressed as a single exponential function.

3) When $\vartheta \gg 1$, or $\sqrt{Dt} \gg \Omega a(1+\varepsilon)^2$, the complimentary error function becomes the dominant term, and the effect of grain boundary diffusion could be neglected.

Diffusion along the grain boundary is usually much faster than diffusion in the bulk. Ω, the ratio of the diffusion coefficients of the two, is about 3 to 5 orders of magnitude. Therefore, most diffusion experiments fall in the first regime. However, when diffusion temperatures become very high, the bulk diffusion coefficient increases with temperature much faster than the grain boundary diffusion coefficient does. Therefore, Ω may become rather small at very high temperatures. Under this condition, diffusion profiles may fall into the regime (2) or (3). Therefore, a pure exponential distribution or pure bulk diffusion profiles may be observed in some high temperature diffusion experiments in polycrystalline materials.

Equation (3.6) is based on the boundary condition that the concentration at the surface is kept constant. When the boundary condition is that the amount of diffusing

solute in the material is fixed, one should expect that the profile would still be the combination of the result of bulk diffusion and grain boundary diffusion [SU64]. The expected bulk diffusion profile is a Gaussian function--according to Suzuoku's result [SU64]--the grain boundary diffusion is still the exponential function. Therefore, the average concentration distribution is expected to be given as follows:

$$\overline{C}(y,t)/C_0 = (1-k)\exp\left(-\frac{y^2}{b_1^{\,2}}\right) + k\exp\left(-(y/b_2)^{1.15}\right). \tag{3.9}$$

The above results and discussion are based on a simplified polycrystalline structure. Because fluorine transport in flint mineral could be conceived as the combination of fast diffusion in the void network and slow diffusion in the bulk, the pipe diffusion model should be applicable in this situation. However, it was found that the surface boundary condition is continuously changing in the flint uptake process; in this case an as yet undefined dynamic boundary condition should be applied in this pipe diffusion model to simulate adequately the fluorine uptake phenomenon. Nevertheless, the empirical forms (3.6) and (3.9) have been shown in this work (see chapter 4, 5) to fit the experimental data very well [JI97a].

CHAPTER 4

EXPERIMENTAL METHOD

This chapter describes various aspects of the experiment. The characterization of sample materials using Scanning Electron Microscopy (SEM), Transmission Electron Microscopy (TEM) and X-ray Fluoresces (XRF) is first discussed. The development of the Nuclear Reaction Analysis (NRA) experimental method is described in detail. A data reduction computer program using two different methods (convolution fitting and deconvolution) is discussed. Other ion beam analysis methods used in this study is then briefly described. Finally, an error analysis is given.

4.1 Sample Preparation

4.1.1 Sample Materials

The primary material used in this study is the commercially supplied "Alibates" flint mineral from a single formation in the Amarillo region of Texas, USA. This flint (or chert) is of non-organic petrogenesis. It is easily identified by its agate-like coloration. The formation has been mined for several millennia. Archeological finds associated with this formation are preserved at the Alibates National Monument, Fritch, Texas [NA00].

The typical microstructure of flint or chert is reported to be granular micro-quartz cemented with amorphous silica containing water [GR94, SH72]. Scanning Electron Microscopy (SEM) and Transmission Electron Microscopy (TEM) have been performed

to study the microstructure of the Alibates flint. Fig. 4.1 and Fig. 4.2 show typical

images of the Alibates microstructure. Both the SEM and TEM images show that the

Alibates flint is composed of two different phases, while the TEM image displays the

structure of micro grains cemented with an amorphous structure. This result is consistent

with other microstructural analyses of flints and cherts of a variety of origins. Both the

enlarged amorphous-phase images from SEM and TEM show that this is a porous

structure. The SEM image shows especially a structure similar to that of amorphous

"potch" opal [GR94]. Potch opal consists of randomly close-packed aggregates of silica

spheres with water filling the interstitial space. This is distinguished from "precious"

opal only by the latter's regular stacking of the silica spheres. It is this regularity that

produces the three dimensional optical grating responsible for the "fire" of the precious
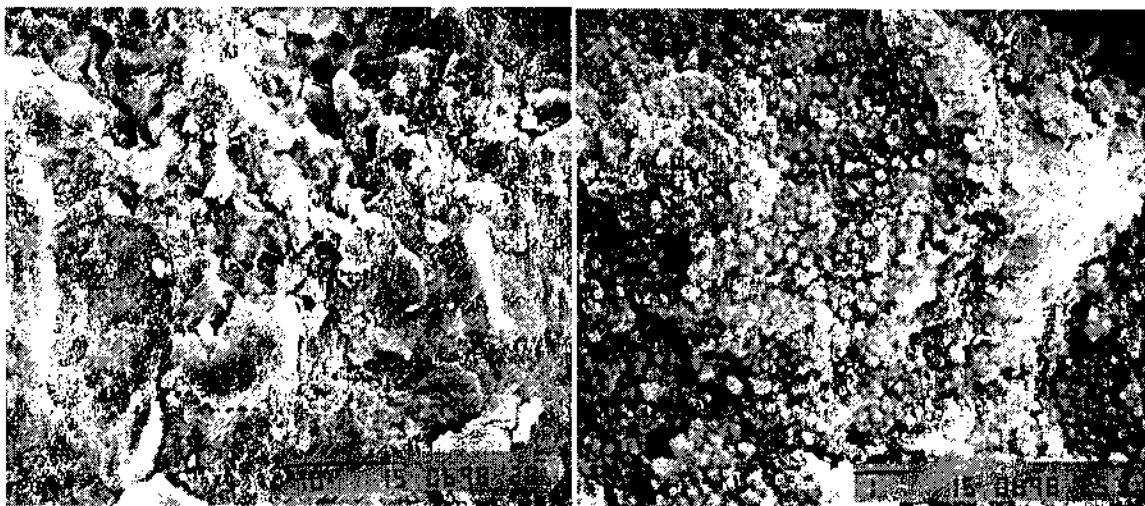
Fig. 4.1, SEM images of the microstructure of Alibates flint. The left picture is a
typical SEM image of a flint sample, which shows two different phases. The right
one shows the amorphous structure, which is composed of randomly stacked
spheres. The scale bars are labeled in units of microns

opal. It has been also reported that opal structures were found in flint minerals of other

origins [SH72].
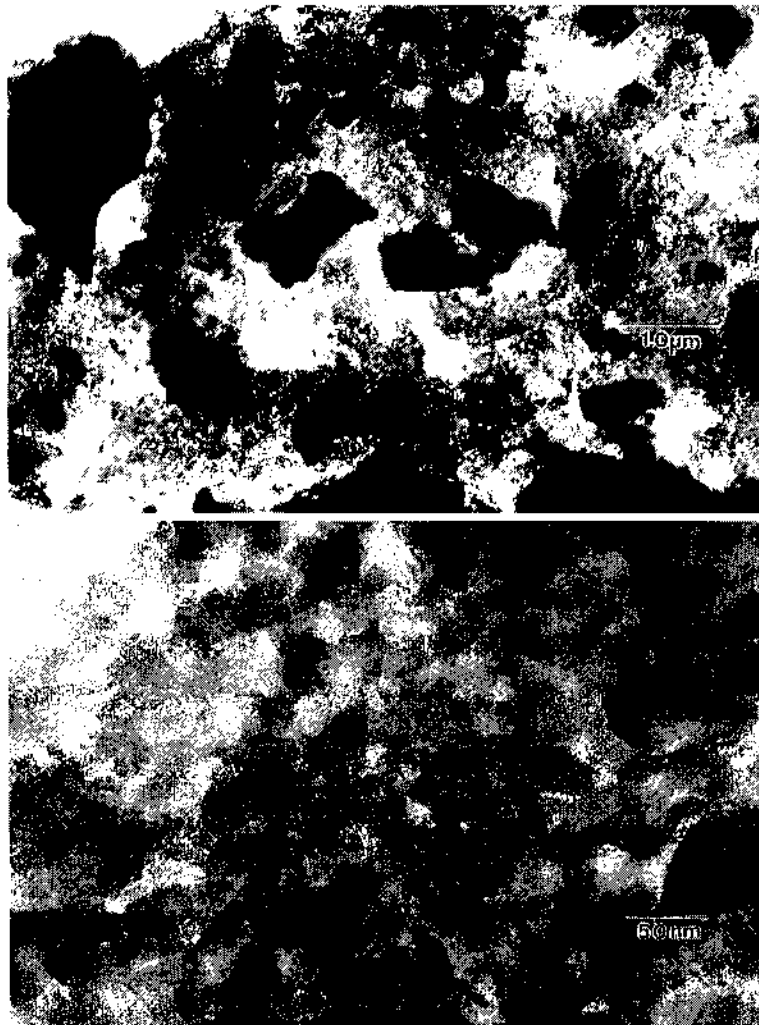
Fig. 4.2, Typical TEM pictures of Alibates flint samples. The top figure
shows a structure of granular crystals cemented with amorphous structures.
The bottom figure shows that the amorphous phase has a porous structure.

This microstructrual picture of Alibates flint is also supported by the following analyses and measurements of density and dehydration. The fractional free volume of a hexagonal close packed (hcp) or a face centered cubic (fcc) arrangement of identical silica spheres is 0.26 [CO93]. Given that the bulk density of hydrated precious opal is approximately 2.20 gm/cm^3 [WE70], and that the micro interstices of the silica-sphere array are filled with water, the density of the silica sphere itself is estimated to be 2.62 gm/cm^3, only about 1% less than the density of quartz (2.65 gm/cm^3) [WE70].

The density of Alibates flint was determined by weighing rectangular parallelepipeds of various dimensions sawed from hydrated samples of the mineral. The volume was calculated from dimensions obtained using micrometer calipers. The bulk density of hydrated samples of the Alibates flint was measured to be 2.48 ± 0.05 gm/cm^3. This is consistent with a volume fraction of micro-crystalline quartz (ρ = 2.65 gm/cm^3 quartz) of 63% and a complementary component of hydrated amorphous silica with a potch-opal-like microstructure (ρ = 2.20 gm/cm^3). Upon dehydration via vacuum baking at 100 °C or annealing at 500 °C in air, the samples were shown to contain approximately 4% water by weight or a free volume of approximately 9.5%. These observations are consistent with the volume fraction of approximately 37% for the amorphous silica, 26% of which is interstitial volume.

X-ray diffraction study has also been performed. The results revealed that α-quartz is the only crystalline phase present in the Alibates samples. Moreover, X-ray fluorescence (XRF) measurements show that the mineral's major constituents are silicon and oxide in the stoichiometry of silica (SiO_2). No measurable difference in Si

concentration compared to a standard quartz sample was found. X-rays from [55]Fe (5.89

keV) and [109]Cd (22.1 keV) were used as excitation sources in the XRF measurements.

Fig. 4.3 shows the typical XRF spectra of Alibates flint. The spectra were compared to

the spectra from a standard sample with about 95 wt% of SiO_2 and 1 wt% or 0.5 wt% for

each impurity element. It was found that Iron (Fe) (about 0.1 wt%) and Calcium (Ca)

(about 0.05 wt%) were the major impurities with the exception of water, which is not

detected well by XRF. Other impurities such as K, Cl, Ge, As, and Br were all found to

be below the level of 100 ppm.
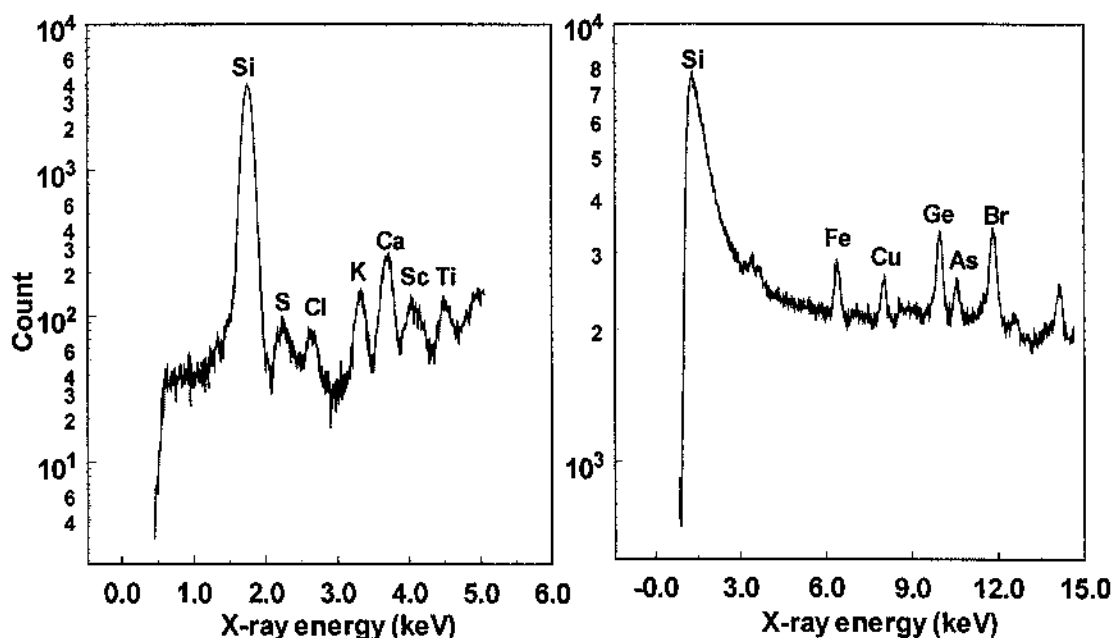
Fig. 4.3, Typical XRF spectra of Alibates flint samples. The left figure is the XRF
spectrum from a 5.89 keV [55]Fe source. The right one is from a 22.1 keV [109]Cd source.

4.1.2 Fluorine Uptake Process

The behavior of other forms of silica, namely, single crystal quartz, poly-crystalline quartz and fused quartz, was also examined as a control in the experiments. All sample materials were cut into about 2 cm × 1 cm × 1 mm pieces with a rock saw. After cutting, the samples were washed with soap and rinsed and finally washed in an ultrasonic bath, first in methanol and then in distilled water.

Fluorine uptake processing was carried out by immersing samples in a series of sodium fluoride (NaF) solutions with different fluoride concentrations at different temperatures for different times. The NaF solution was made by dissolving NaF powder in deionized distilled water. A buffer solution was added to keep a constant pH value. The constant temperature of the solution was maintained by placing the container in a thermal bath. The short and long term temperature stability of the thermal bath was better than ± 1.0°C.

4.2 Fluorine Depth Profile Measurement

4.2.1 Nuclear Reaction Analysis (NRA)

The fluorine concentration depth profiles are measured using the $^{19}F(p, \alpha\gamma)^{16}O$ reaction at a proton energy of 872 keV [MA77]. The reaction is expressed as follows:

$$^{19}F + p \rightarrow {}^{20}Ne^* \rightarrow {}^{16}O^* + \alpha, \tag{3.1a}$$

$$^{16}O^* \rightarrow {}^{16}O + \gamma. \tag{3.1b}$$

In this reaction, first a compound nucleus of $^{20}Ne^*$ is first formed, then the unstable $^{20}Ne^*$ dissociates into an α particle and an unstable excited-state $^{16}O^*$ nucleus, and finally the

$^{16}O^*$ decays to its ground state ^{16}O by releasing the energy as γ rays. This reaction is a resonance nuclear reaction; it takes place only when the center-of–mass energy of the proton and fluorine corresponds to the energy level of the excited states of ^{20}Ne. The energy of the released γ-rays corresponds to the energy of ^{16}O excited states. They are 6.13, 6.92 and 7.12 MeV.

Fig. 4.4 shows two typical γ-ray-spectra measured by a NaI detector from the resonance reactions at proton energies of 872 keV and 935 keV, respectively. One sees that the majority of the γ-rays are 6.13 MeV with two escaped peaks. However, the γ-ray spectra for the two resonance reactions are not identical. The resonance reaction at the proton energy of 872 keV produces more γ-rays of 6.92 MeV than γ-rays of 7.12 MeV, while the reaction at 935 keV produces more γ-rays of 7.12 MeV.

The reaction at a proton energy of 872 keV has a maximum cross section of about 540 mb, with a resonance width of 4.5 keV. This is an ideal resonance reaction for depth profiling measurements due to its relatively high cross section, narrow resonance width and low background noise at this high energy [MA77, JI97a]. However, the existence of other resonances in the neighborhood of the primary peak may limit the range of depth measurement.

Fig. 4.5 shows the measured reaction cross section versus the proton energy in the energy range of interest. The figure shows that in addition to the resonance reaction at 872 keV, there are a small resonance at about 902 keV and another rather large resonance at about 935 keV. In section 4.3, a computer program that corrects for the interference of these neighboring resonances as well as other effects is discussed.
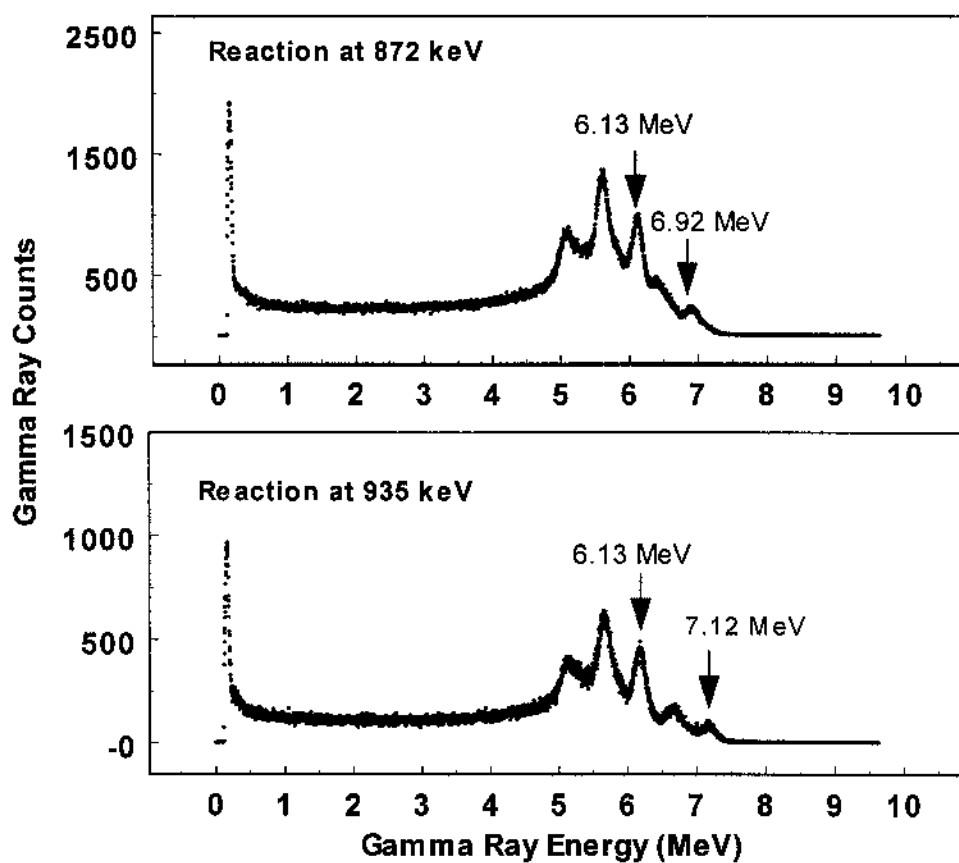
Fig. 4.4, γ-ray spectra form the $^{19}F(p, \alpha\gamma)^{16}O$ reaction. The top figure is the spectrum for the resonance reaction at a proton energy of 872 keV. The bottom one is the spectrum for the resonance at a proton energy of 935 keV.
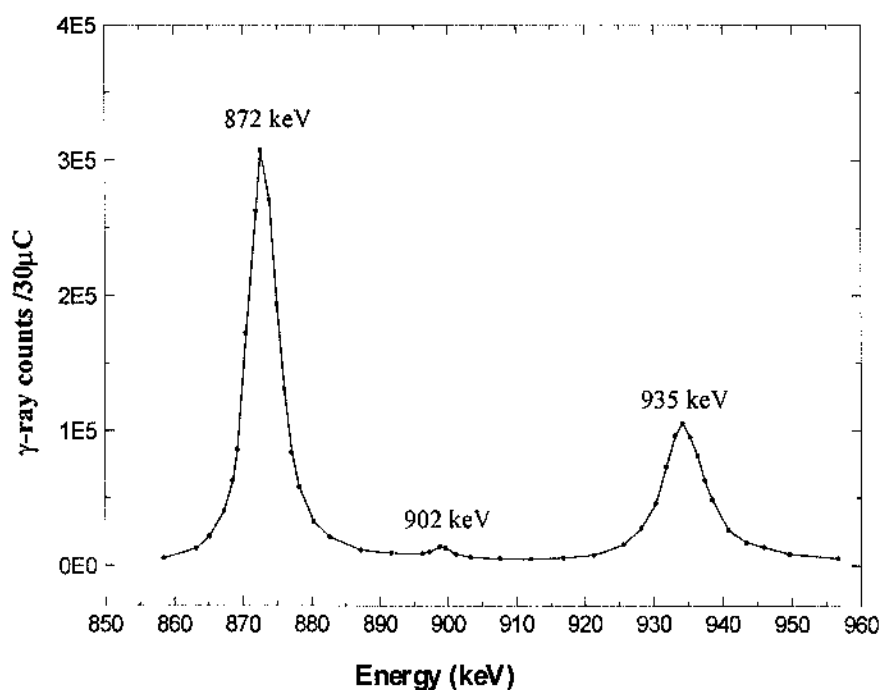
Fig. 4.5, $^{19}F(p, \alpha\gamma)^{16}O$ resonance nuclear reaction excitation curve for a proton energy range of 850 to 960 keV. Three resonances are in this range.

The amount of fluorine in a sample is determined by measuring the γ rays of the reaction. In depth profile measurements, the energy of the proton beam is scanned in small steps around the resonant energy. The corresponding γ ray count for each energy step is recorded. Due to the energy loss of the proton beam in inelastic interactions with the atoms in the sample, the proton energy decreases as it travels deeper into the sample. A higher incident proton beam energy corresponds to a larger depth where the beam reaches the resonant energy for the nuclear reaction. Therefore, the plot of γ ray counts versus incident proton energy is an indication of the fluorine concentration distribution in

depth. A detailed recovery of the fluorine depth profile from the measured raw data is discussed in section 4.3.

4.2.2 NRA Experiment Set up

The proton beam is provided by the 3 MeV tandem accelerator at the Ion Beam Modification and Analysis Laboratory (IBMAL) at the University of North Texas. The experimental set up is shown in Fig. 4.6. A negative hydrogen ion beam is produced from the Source of Negative Ion by Cesium Sputtering (SNICS), and is injected into the tandem accelerator. The negative ions are stripped off two electrons at the terminal gas stripper and become positive ions, which are accelerated to the final energy of about 872 keV. The beam is then bent by the analyzing magnet into the sample chamber.
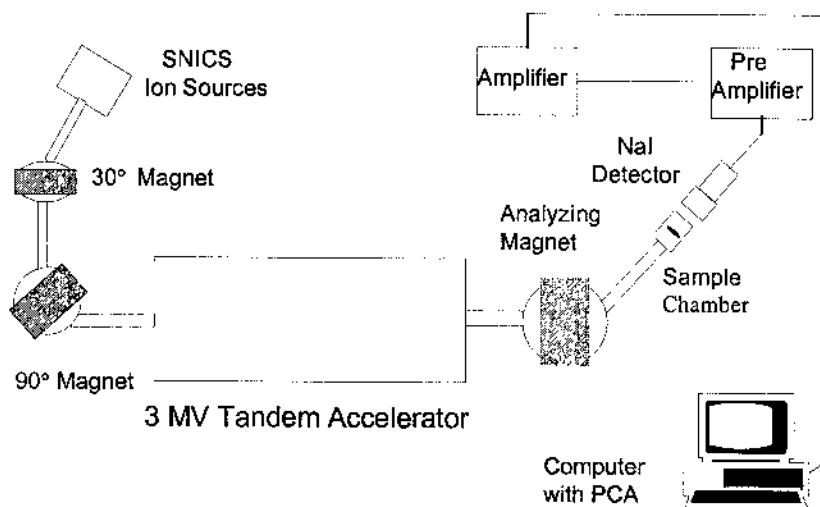
4.6, Schematic drawing of the NRA depth profile experimental arrangement.

The proton beam current in the target is maintained at about 50 nA with a beam spot about 3 mm in diameter. A 3 in × 3 in NaI scintillation γ-ray detector is placed outside the chamber and records the γ-ray counts. The selected γ-ray energy window is about 4.5 to 7.5 MeV. The magnet is adjusted at each energy step to insure that the beam is centered in the slits. The focusing component (an electrostatic quadrupole doublet) is automatically adjusted to keep the beam size constant when the energy is varied.

4.2.3 Surface Charging Problem

Because flints and other materials used for the experiment are insulators, the surface of the sample may be charged to a high positive potential by the incident ions and by ejected second electrons. It has also been suspected that an internal high potential distribution may be built up due to the charged ion beam interaction. The existence of the surface or internal potential will reduce the proton beam energy, and an unstable surface potential may cause the depth profile measurement to be unreliable.

To examine the influence of the surface charging effect on the measurement, the resonance peaks of the proton beams in a very thin layer of CaF_2 evaporated on the surfaces of a conductor substrate and an insulator substrate were measured and compared. The surface charging would be indicated by a shift of the resonance peak to higher energy while an unstable surface potential would cause the peak to broaden or would destroy the shape of the Lorenzian resonance peak.

The influence of the incident beam current was also checked by varying the beam current from 5 nA to 200 nA with about a 1.5 mm × 1.5 mm beam spot size to test for

change in the resonance peaks. It is found that the resonance peak did indeed shift a few

keV for the insulator sample (100 Å of CaF_2 evaporated on a cut flint substrate)

compared to the peak for a conducting sample (100 Å of CaF_2 evaporated on a tantalum

substrate). However, the peak is still well shaped. Fig. 4.7 shows the relation of peak

shift (or surface potential) versus the beam current. The peak shift increases as the beam

current increases, but the curve seems to be irregular. However, when the surface

conductivity (current/surface potential) is plotted versus current, it is interesting to note

that the surface conductivity increases linearly as the beam current increases.
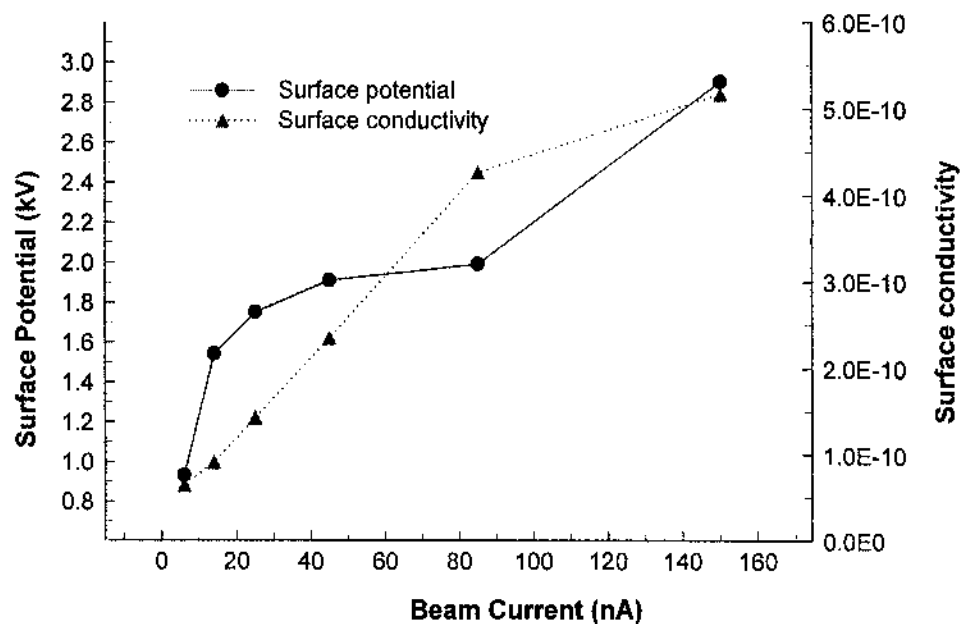
Fig. 4.7, Surface potential and surface conductivity versus beam current on a rock-saw-cut flint sample evaporated with 100 Å of CaF_2 in NRA measurement.

This suggests an ion-beam-induced enhancement of the surface conductivity of the insulator materials. The possible explanation of this phenomenon is that the ion bombardment produces electron-hole pairs in the insulator material, which enhances the conductivity.

To check the possible effect of internal charge, two samples were prepared by evaporating 100Å of CaF_2, 2000 Å of SiO_2 and 200Å of Al onto substrates of tantalum and cut flint, respectively, and these samples were measured to compare their resonance peaks. It is found that the two peaks are almost identical, indicating that the internal charge effect is negligible.

The surface charging effect in quartz samples (polycrystalline, single crystal or fused quartz) is very severe if care is not taken. The surface potential can charge up to 10 kV, with the result that the resonance shape is totally destroyed (see fig. 4.8). This problem was resolved by using the mesh method. In this method, the insulator surface was first covered with a 98% transparent copper mesh, and then a piece of aluminum foil was placed over the mesh. A small hole in the foil was centered on the mesh, and the foil was then wrapped around the sample to secure the mesh by its edge (see Fig. 4.9). With the mesh, the surface potential is reduced to about 2 keV with beam currents of 60 nA (see Fig. 4.8). Another method such as coating the surface with a thin carbon or gold layer is also a general method to solve this problem. However, because coating itself introduced some unknown energy loss and energy straggling, and the procedure is not as simple as the mesh method, the mesh method was preferred in this study. The mesh method was also used for flint samples. It was found that by use of the mesh, the peak shift for the flint samples was

reduced to about 200 eV, which is negligible in comparison to the energy stability of the

accelerator.
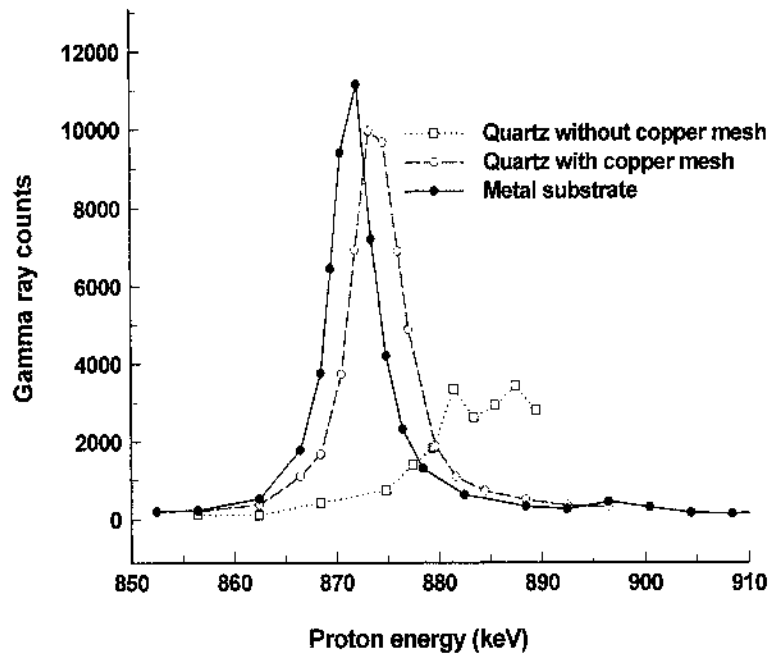
Fig. 4.8, Surface charging in a quartz sample. The meshed quartz sample has about 2.5 keV peak shift, while for the unmeshed sample the peak is totally destroyed.

Fig. 4.9, The insulator sample is first covered with copper mesh and then covered by an Al foil with a window

4.3 Data Reduction --- Numerical Methods in Fluorine Depth Profiling

4.3.1 General Description

As mentioned in the last section, in fluorine depth profiling, the measured raw data

are in the form of the γ-ray yield curve, $Y(E)$ (γ-ray counts versus incident proton energy).

The fluorine concentration distribution, $C(x)$, is related to $Y(E)$ in the following convolution

expression [MA82, BO82, DE83]:

$$Y(E) = \int_0^\infty C(x)G(E,x)dx, \qquad (4.2)$$

where $G(E, x)$ is the probability for an incoming proton particle of energy E to produce a

detected γ-ray count for unit concentration in the vicinity dx of depth x. $G(E, x)$ can be

referred to as the thick target excitation function or general excitation function. Although

in principle, $C(x)$ can be determined by solving equation (4.2) if $G(E, x)$ is known, it rarely

has an analytical solution, because $G(E, x)$ is a very complicated expression. Numerical

methods are usually required for the solution to the problem. Two numerical methods,

namely, the convolution fitting and deconvolution methods, are developed to unfold the

$C(x)$ from $Y(E)$. For the first step, a reasonably simplified expression of $G(E, x)$ have to be

determined.

4.3.2 $G(E, x)$ Determination

The general excitation function $G(E, x)$ itself is the convolution of the reaction cross

section $\sigma(E)$ with the proton energy distribution caused by the intrinsic beam energy spread

and by the energy straggling inside the target, multiplied by the factors of detector

efficiency and solid angle [MA77]. $\sigma(E)$ can be experimentally determined by measuring

the thin target excitation function $g(E)$ (or simple excitation function), and is closely

approximated by a Lorenzian function according to the Breit-Wigner formula [SE53]. The

energy spread from the energy straggling and the instruments are close to a Gaussian.

Therefore, $G(E, x)$ could be approximated as a Pearson function, because the convolution

of a Lorenzian with a Gaussian can be represented accurately by the Pearson function

[JA95]. The general exitation function can thus be written in the following form:

$$G(E,x) = \frac{A_0 A(x)}{\left(1 + 4\left(\frac{E-E(x)}{D(x)}\right)^2 \left(2^{1/a(x)} - 1\right)\right)^{n(x)}} .$$ (4.3)

The detailed expression for $G(E, x)$ was determined by the following experiment: a

very thin layer of calcium fluoride (100 Å) was evaporated onto a Si wafer followed by

evaporation of another layer of SiO_2 with thickness x_1. Then the γ-ray yield curve for this

sample was measured. It closely represents $G(E, x)$ because SiO_2 is the main component of

flints, although the evaporated SiO_2 is expected to be amorphous while flint is a mixed

structure of polycrystalline and amorphous silica. Then samples with different SiO_2

thicknesses x_i were measured and $G(E, x_i)$ was determined. Fig. 4.10 shows these

measured $G(E, x)$ peaks. It was found that all the peaks are well fitted to the Pearson

functions, while they are not matched by either Lorenzian or Gaussian functions. Finally,

the detailed expression of $G(E, x)$ was determined by linearly fitting $D(x_i)$ and $a(x_i)$.

It must be noted that the resonance peak at 872 keV has two adjacent resonances at

902 keV and 935 keV. Observing that the stopping power of SiO_2 for protons of energy

near 900 keV is about 52 keV/μm, this suggests that when measuring the fluorine

concentration at depths larger than 0.5 μm, γ-rays from these two adjacent peaks may

interfere with the measurement. Therefore, the final excitation function $G(E, x)$ includes all

three Pearson peaks corresponding to the three resonances in Fig. 4.5 in order to accurately

represent reality. That is,

$$G(E, x) = G_1(E, x) + G_2(E, x) + G_3(E, x), \qquad (4.4)$$

where $G_i(E, x)$ has the form of equation 4.3.
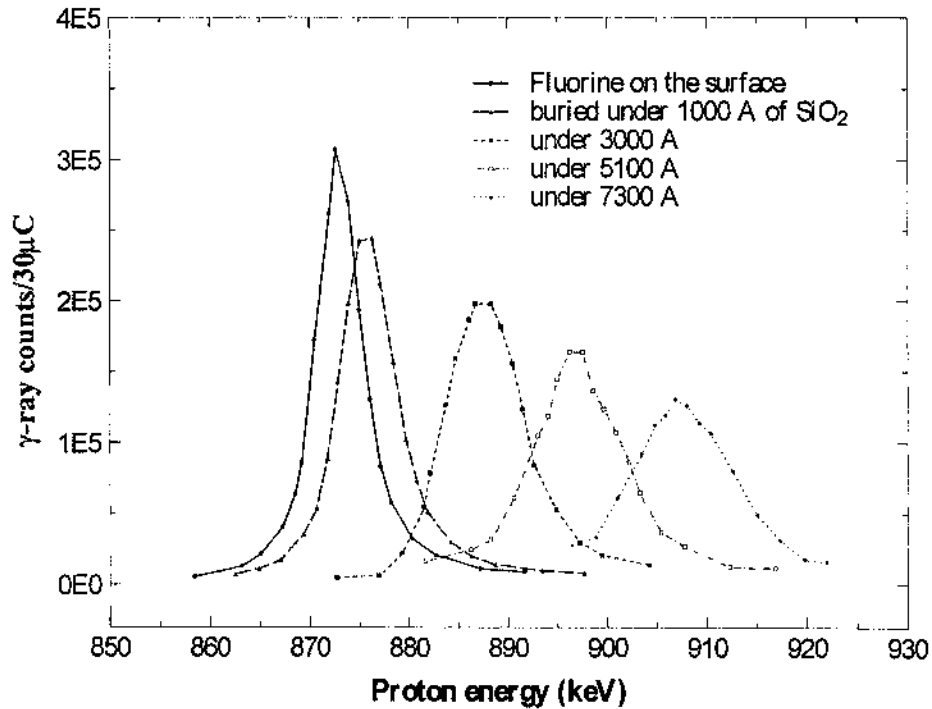
Fig. 4.10, Resonance peaks of 100 Å of CaF$_2$ on a Si wafer covered with a SiO$_2$ layer of different thickness.

4.3.3 The Convolution Fitting Method

The convolution fitting method is similar to other standard fitting methods. It first assumes a parameterized concentration distribution $C(x, p)$. Then it uses a fitting algorithm to determine the optimal parameters, and the concentration distribution is hence determined [RE92]. The following is a brief description of this method:

(1) Assuming that the fluorine depth distribution is $C(x, \mathbf{p})$, where $\mathbf{p}$ is the parameter vector, then the expected value of γ-ray counts $Y_{th}(E_k, \mathbf{p})$ at each energy point E_k is calculated as:

$$Y_{th}(E_k, \vec{p}) = \int_0^\infty C(x, \vec{p}) G(E_k, x) dx. \tag{4.5}$$

(2) Define the function $F(\mathbf{p})$ as the sum of the squares of the difference between the expected value and the experimental value for all the energy points:

$$F(\vec{p}) = \sum_{E_k} \left(Y(E_k) - Y_{th}(E_k, \vec{p}) \right)^2. \tag{4.6}$$

(3) Find the optimal value $\mathbf{p}_{opt}$ to minimize $F(\mathbf{p})$ using the Levenberg-Marquardt compromise algorithm [RE92].

A correct concentration distribution model $C(x, \mathbf{p})$ is the key to the success of this fitting method. Different models should be used for different diffusion conditions. The complimentary error function $p_1 \text{erfc}(x/p_2)$ is certainly the correct model to use for bulk diffusion within a constant fluorine concentration environment. The Gaussian function $p_1 \exp(-x^2/p_2^2)$ would be the right choice for bulk diffusion of a thin layer of fluoride. As

discussed in chapter 3, the combination of a complementary function and an exponential function,

$$F(x) = p_1 erfc(x / p_2) + p_3 \exp(-x / p_4)$$ (4.7)

is a model for diffusion in polycrystalline materials. However, when the diffusion mechanism is unknown or abnormal, general models such as

$$F(x) = p_1 + p_2 x + p_3 x^2 + p_4 x^3,$$ (4.8)

or

$$F(x) = p_1 \exp(-x / p_2) + p_3 \exp(-x^2 / p_4^2)$$ (4.9)

should be used. Fluorine diffusion in flint is more complicated than diffusion in polycrystalline materials. However, it is also similar to diffusion in polycrystalline material, and can be closely approximated by the pipe diffusion model. Therefore, equations (4.7) and (4.9) were used as the trial models in this study. It turned out that these two models can fit the experimental data very well [JI97a]. The normalized standard deviation was generally less than 5% using the convolution fitting.

4.3.4 The Deconvolution Method

The deconvolution method is the direct recovery of the best estimation of $C(x)$ from $Y(E)$ using Jansson's iterative algorithm [BL81]. For the convolution relation (4.2), the deconvolution iteration relation is

$$C_n(x) = C_{n-1}(x) + \lambda(C_{n-1}) \frac{\varepsilon(E)}{A_0} \left(Y(E) - \int_0^\infty G(E, x) C_{n-1}(x) dx \right) \Bigg|_{E = E_R + \varepsilon(E)x}.$$ (4.10)

Here A_0 is the area of the major resonance peak. $\varepsilon(E)$ is the average stopping power. $\lambda(C)$ is a relaxation factor that ensures the iteration will be convergent. It is expressed as follows,

$$\lambda(C) = 1 - 2\left|\frac{C(x)}{C_{max}} - \frac{1}{2}\right|.$$

(4.11)

The subscript n in $C_n(x)$ denotes the number of iterations. The starting value $C_0(x)$ is formed by assuming $G(E, x)$ to be a δ function, which gives:

$$C_0(x) = \left.\frac{\varepsilon(E)}{A_0} Y(E)\right|_{E=E_R+\varepsilon(E)x}.$$

(4.12)

Each iteration produces a correction that takes into consideration the contribution caused by the spread of the actual excitation peak $G(E, x)$.

This iterative relation requires continuous $Y(E)$ data, or at least a very narrow interval E_k between points, to ensure that the calculation of the integral is precise. The experimental data are sometimes very sparse. A Lagrange interpolation scheme is used to interpolate the value between two data points and smoothly connect them to other data points [GE70].

This deconvolution method is usually found to be convergent. After about 10 iterations, the standard deviation (or sum of squares) would decrease to a small value. The normalized standard deviation would go down to about 5%. If $C(x)$ is reconvoluted back with $G(E, x)$, it fit the experimental data $Y(E)$ with little deviation.

4.4. Other Experimental Methods

In addition to the NRA method that was used to measure the fluorine depth profiles in the samples, a variety of other experimental tools have been used in this study. SEM, TEM and X-ray diffraction were used to study the microstructure of the flint sample. The XRF method was used to study the impurities in the flint sample. The NRA method was also used to study the hydrogen (or water) distribution in the samples. And the Elastic Recoil Detection (ERD) was used to measure the thickness of the SiO_2 film at the Si wafer surface, so that the etching effect of silica in a fluoride solution could be monitored. In this section, the NRA method to measure hydrogen profiles and the ERD method to measure oxygen thickness are briefly discussed.

4.4.1 Hydrogen Depth Profiling by NRA

The NRA method can also be used to measure the hydrogen profiles. The $^1H(^{19}F, \alpha\gamma)^{16}O$ reaction at a fluorine ion energy of 6.42 MeV was used in the measurements. The $^1H(^{19}F, \alpha\gamma)^{16}O$ reaction is basically the same reaction as the $^{19}F(p, \alpha\gamma)^{16}O$ reaction, except that it uses fluorine ions to strike samples with hydrogen instead of using protons to hit samples with fluorine. These two reactions require the same kinetic energy in the center-of-mass reference system to trigger the resonance reaction. Therefore, in the lab reference system, the energy of fluorine ions must be 19 times the energy of the protons to produce the same reaction. The reaction at a fluorine ion energy of 6.42 MeV corresponds to the reaction at a proton energy of 340 keV, which has a cross section of 160 mb and resonance width of 3 keV of proton energy. The reaction that we

used in fluorine depth profiling at the proton energy of 872 keV corresponds to a fluorine

ion energy of 16.44 MeV. The reaction at a fluorine energy of 6.42 MeV was selected to

measure hydrogen profiles because 6.5 MeV fluorine ions are much easier to be accelerated

with the 3 MV tandem accelerator, and this reaction has a narrow resonance width.

The experimental set-up and all the concepts related to depth profiling are similar to

that of NRA in fluorine depth profiling.

4.4.2 Elastic Recoil Detection of Oxygen

ERD is an important method for measuring hydrogen and other light elements in

the near surface region of materials with a smooth surface [BA95, DO79]. The principle

behind ERD is quite similar to Rutherford Backscattering Spectrometry (RBS). Instead

of measuring the back scattering particles in RBS, the forward recoiling particles that are

knocked out by the incident heavy ions are measured. Fig.4.11 shows schematically the

simple experimental arrangement. The sample is tilt mounted so that the recoil particles

can come out from the surface. The detector that measures the energy of recoiled

particles is usually placed at a small detection angle in the froward direction. A thin foil

of proper thickness is placed before the detector to stop the large number of scattering

ions. The foil should be thick enough to stop the scattering heavy ions, but thin enough

to let the recoiling particles go through with minimal energy loss and energy straggling.

ERD was used to measure the amount of oxygen in the thin film of SiO_2 on a Si

wafer sample in this study. By measuring the amount of oxygen in a SiO_2 film before

and after it is immersed in a fluoride solution, one can monitor the etching effect of SiO_2

in the fluoride solutions. The RBS method can also be used to measure oxygen, but

because of the large background of α particles scattered by Si atoms, the sensitivity of

detecting oxygen in a Si wafer is not satisfactory. There are certainly other methods such

as ellipsometry that have very high sensitivity to measure the thickness of a thin film

[WA93]. However, ERD as an important ion beam analysis method, is worthwhile for

further development.
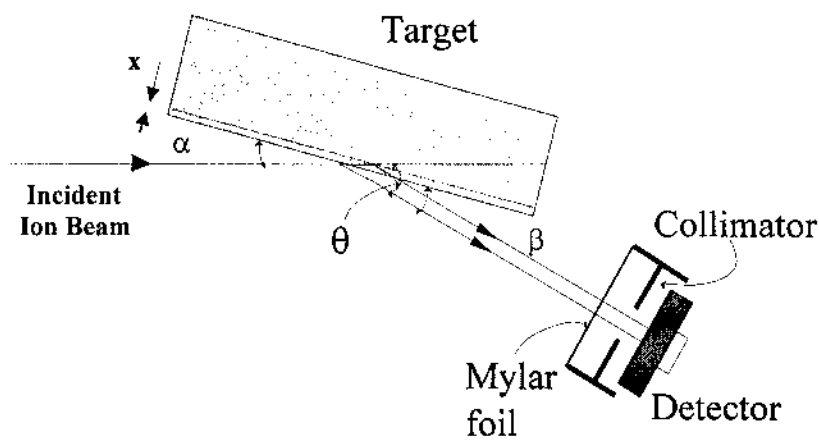
Fig.4.11, Schematic drawing of the ERD experimental arrangement.

The 14.0 MeV Si^{5+} ions from our 3 MeV tandem accelerator were used as the

incident ion beam. Fig 4.12 shows ERD spectra of 14.6 MeV Si ions on 800 Å and 254 Å

SiO_2 films, and spectra of 14.0 MeV Si ions on the 254 Å SiO_2 film before and after being

immersed in NaF solutions for 4 days. One can see that the oxygen peak is well separated

from the hydrogen peak. With proper cross section correction, the amount of oxygen in the

sample can be determined by the total counts of the oxygen peak. When the SiO_2 is less

the 250 Å, the amount of oxygen is linearly proportional to the total counts of the oxygen

peak.
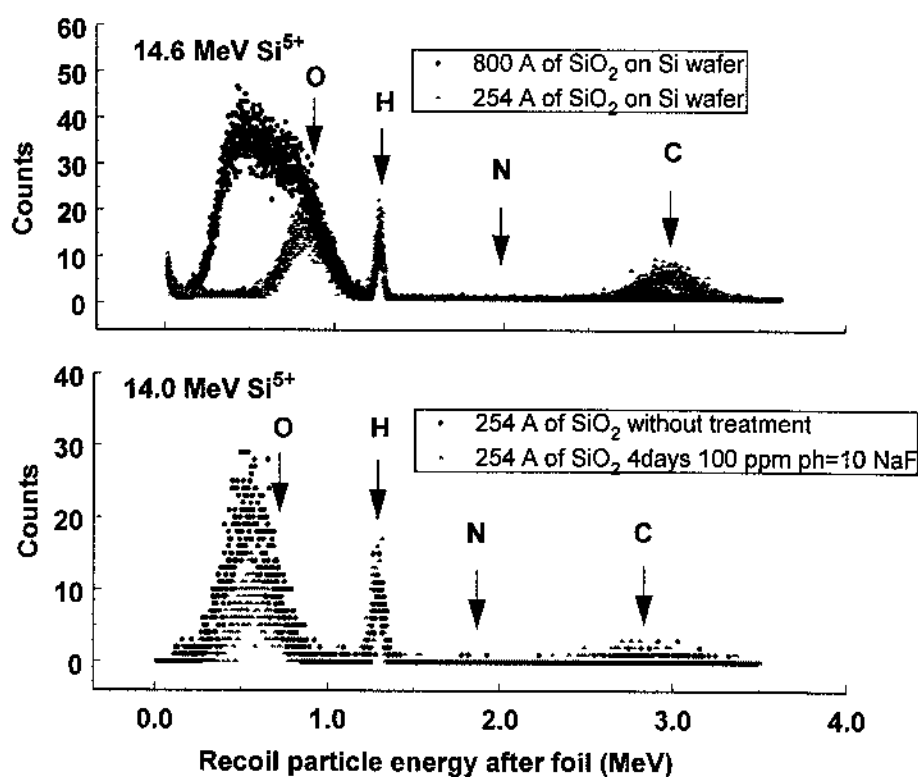
Figure 4.12, ERD spectra of Si ions in SiO_2 films on Si wafers. The top figure shows the spectra using 14.8 MeV Si ions as the incident ions in 800 Å and 254 Å SiO_2 films. The bottom one shows the spectra using 14.0 MeV Si ions in 254 Å of SiO_2 without and with 4 days in the 100 ppm NaF solution of pH=10 and temperature =80°C

4.5 Error Analysis

There are three sources of error in this study. One source of error is the experimental simulation process of fluorine uptake, which includes the fluctuation of different parameters such as temperature, fluoride concentration, etc. Another source of error is the measurement process. Nuclear Reaction Analysis (NRA) and other ion beam analysis methods introduce errors. The third source of error is the data reduction process through the convolution fitting and deconvolution methodology. This section discusses and evaluates errors in these three different processes.

Errors are usually classified as two different types, the systematic error and the random error. A systematic error is one that is due to a definite identifiable cause such as an error in the charge normalization in the ion beam analysis. Systematic errors are usually constant and repetition of experiments would not give different results. On the other hand, random errors are due to unknown causes, usually large in number and acting in different ways. Random errors can be reduced by a large number of repetitions of experiments. If a quantity Q is the function of several parameters, $Q = f(x, y, z.....)$, then the errors in parameters x, y, z can be propagated to Q and the error of Q is [MA86]

$$\delta Q = \sqrt{\left(\frac{\partial f}{\partial x}\right)^2 (\delta x)^2 + \left(\frac{\partial f}{\partial y}\right)^2 (\delta y)^2 + \left(\frac{\partial f}{\partial z}\right)^2 (\delta z)^2 + ...} \ . \qquad (4.13)$$

4.5.1 Error in the Uptake Simulation

In the present study, the amount of fluorine adsorption and the depth of fluorine penetration are two important quantities of interest. The fluctuation of different

parameters in the simulation greatly affects these two quantities. These parameters include temperature, fluoride concentration in the solution, pH value, impurity levels in solution and in the sample, microstructure of the sample and other unknown parameters. The fluctuation of temperature is caused by the instability of the thermal bath, which is within $\pm 1°C$. The pH value is well controlled by adding a buffer solution. Fluoride concentration in the solution is affected by evaporation of water and adsorption of fluorine by the sample and container wall in the uptake process. The container is well covered by aluminum foil to avoid water evaporation. However, other parameters such as impurity levels and microstructures of the samples are difficult to control and evaluate.

Equation (4.13) suggests that the error of a quantity is not only dependent on the fluctuation of the parameters that relate to the quantity, but also dependent on the partial derivative of the quantity with the parameters. A parameter which has a strong relation (sharp slope or large partial derivative) to the quantity could contribute a large error to the quantity even if its fluctuation is small. However, the relations of the quantities of interest to the parameters in this study are not known and are subject to investigation. A quantitative evaluation is rather difficult to make. Nevertheless, as it will be discussed in the next chapter, the amount of fluorine adsorption is strongly dependent on the Ca^{2+} impurity levels in the solution. Because Ca is also a major impurity in the flint samples, the inhomogeneous distribution of Ca within the sample and among the different samples may dominate the error of fluorine adsorption.

4.5.2 Error in the Measurement

NRA and ERD are well-established ion beam analysis methods. The error of the measurements can be well evaluated. The major error is the random error from the detection system. A reasonably large number of counts reduces the statistical error. In NRA measurements, the γ-ray count for each data point is larger than 1000, which has the statistical error of 3.2%. However, there are several sources of typical systematic error in ion beam analysis. The charge normalization of the ion beam by the faraday cup is usually the most typical source of error. Ejected high-energy electrons, photon and X-ray induced electrons and sputtered ions will not be confined by the suppressor in the faraday cup and hence error is induced. Davies et al. reported that the maximum effect of error caused by high-energy electron ejection is about 1-2%. The effect of X-ray-induced-electrons is about 0.1% for metal targets, while it is larger than 100% for polymers. The effect of sputtered ions is negligible for high energy (MeV) ions such as 870 keV protons and 14 MeV Si ions used in this study [DAV95]. Another effect on charge normalization is charge exchange in the beam line, especially when the vacuum is not very good. This effect is negligible in NRA because the proton has only one charge-state. This effect seems quite large in ERD because a Si^{5+} beam was used. 5%-10% current variations are observed using a monitor cup in the ERD measurements.

Another source of systematic error is the uncertainty associated with the standard sample. In this NRA measurement, a sample of 200 Å CaF_2 evaporated on a silicon wafer is used as the standard. The error of thickness is estimated to be about 5%. Other sources such as the background of γ-ray irradiation from other reactions, the radiation

damage of the sample, and the charging effect of the sample all contribute to the errors. The overall systematic error in the measurement is expected to be in the range of 5% to 10%. No error bars are drawn in the fluorine uptake results in the next chapter because the error from the fluorine uptake experiment is larger than the error from measurement and is not easy to estimate.

4.5.3 Error in the Data Reduction

Because convolution fitting and deconvolution methods have been used to recover the fluorine depth profiles from the measured γ-ray yield curves, errors are also introduced in this data reduction process. Both convolution fitting and deconvolution methods use the Sum of Squares due to Error (SSE) as the criterion. SSE is defined as

$$SSE = F(\bar{p}) = \sum_{E_k} w_k \left(Y(E_k) - Y_{th}(E_k, \bar{p}) \right)^2. \tag{4.14}$$

where w_k is the weight factor ($w_k=1$ is used in the present study), $Y(E_k)$ is the experimental data, and $Y_{th}(E_k, p)$ is the estimated value generated by the model. Each computer program uses an iteration scheme to reduce SSE to a minimum.

The fitting criterion is represented by the coefficient of determination r, which is given by

$$r = \sqrt{1 - \frac{SSE}{SSM}}. \tag{4.15}$$

SSM is the Sum of Squares about the Mean, and is defined as:

$$SSM = \sum_k w_k \left[Y(E_k) - \bar{Y} \right]^2, \tag{4.16}$$

where $\bar{Y}$ is the mean of all the data $Y(E_k)$.

SSE or r sometimes does not reflect the real error for the data reduction program because when the number of parameters is comparable to the number of data points, SSE go to zero, which sets $r = 1$, meaning a perfect fit. A standard error S_E is introduced to represent the error caused by the data reduction program. It is defined as

$$S_E = \sqrt{\frac{SSE}{n-m}} \tag{4.17}$$

where n is the number of data points, m is number of parameters, and n-m is the number of degree of freedom. The Normalized Standard Error (NSE) is then defined as

$$NSE = \frac{S_E}{\sqrt{SSM/n}} = \sqrt{\frac{SSE \cdot n}{SSM \cdot (n-m)}} \tag{4.18}$$

The calculated normalized-standard-error is about 5% in both convolution fitting and deconvolution programs used to evaluate the fluorine depth profiling data. The fluorine adsorption data are not subjected to this error.

CHAPTER 5

RESULTS AND DISCUSSION

In this chapter, all the experimental results related to fluorine uptake are presented

and discussed. First is the comparison of fluorine uptake between a flint sample and

other forms of silica. A time dependent study of fluorine uptake is then discussed.

Results of fluorine surface adsorption under various experimental conditions, such as

different pH values, fluorine concentrations, temperatures and other impurity levels are

discussed. Finally, a study of silica etching in the NaF solution is presented.

5.1 Comparison between Flint and Other Forms of Silica

The first experiment examined the differences between flint samples and other

forms of silica. Samples of flint, mono-crystal and poly-crystalline quartz, and fused

quartz were immersed in a 300 ppm NaF solution and held at 80 °C for 6 days. The

fluorine uptake profiles in these samples were then measured using the NRA method. A

reversed (p, $\alpha\gamma$) nuclear reaction, specifically, the $^1H(^{19}F, \alpha\gamma)^{16}O$ nuclear reaction at a

fluorine energy of 6.42 MeV was also employed to measure the hydrogen concentration

in these samples. The hydrogen distribution should reflect the water concentration in the

samples. The measured results are shown in Fig.5.1. The fluorine profiles are on the left,

and the hydrogen profiles are on the right. The differences between the flint sample and

the quartz samples are very obvious both in their fluorine and hydrogen profiles. The

fluorine uptake in the flint sample is at least 100 times higher than that in other forms of

silica. Moreover, the flint sample shows much more hydrogen inside the bulk, while the

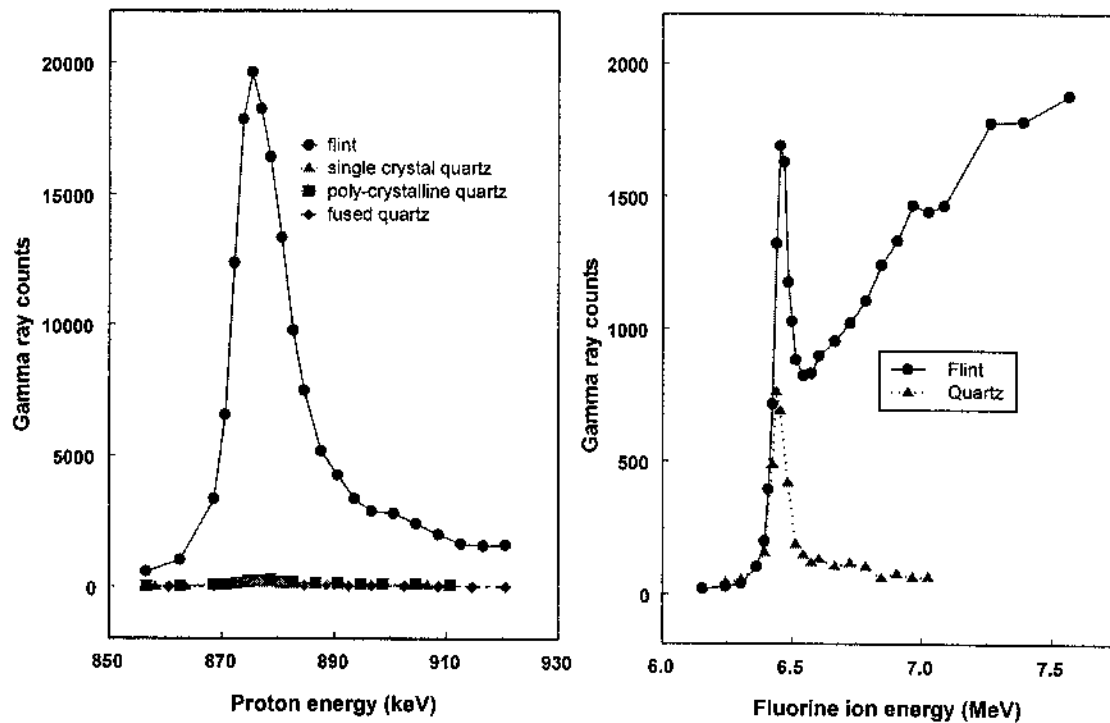quartz sample shows very little internal hydrogen.

Fig. 5.1, Comparison of fluorine profiles and hydrogen profiles between flint and quartz samples. The left figure shows the fluorine profiles measured using $^{19}F(p, \alpha\gamma)^{16}O$ NRA, and the right figure shows the hydrogen profiles measured using $H(^{19}F, \alpha\gamma)^{16}O$ NRA.

It is interesting to note that aside from the hydrogen peak at the surface of the flint sample, hydrogen tends to be less abundant in the near surface, and increases with depth into the bulk. This observation is explained as the result of water loss or dehydration from the open voids in the near surface region when the sample was exposed to air or to the vacuum system. Note that the stopping power of 6.5-7.5 MeV fluorine ions in SiO_2 is about 2.2 MeV/μm; therefore dehydration seems to have taken place mostly in the first 200 nm region near the surface, and extends to 500 nm in depth.

The significant difference in fluorine concentration between flint and other forms of silica suggests that the unique microstructure of flint may account for this fluorine uptake phenomenon, while as revealed in a later section, the impurities in the flint mineral may also play an important role. The hydrogen profile in flint supports an open-void microstructure in flint samples. And because of this open-void structure, fluorine could easily diffuse into the flint bulk through the liquid water present in the open volume.

5.2 Time Dependent Study

A time-dependent study of fluorine uptake has been carried out. Flint samples were immersed in a 300 ppm NaF solution at 80 °C for various times, and then the fluorine profiles were measured using the NRA method. Fig.5.2 shows the results: the left figure displays the measured raw data, or the so-called γ-ray yield curve, and the right figure shows the fluorine depth profiles generated by the convolution fitting computer program mentioned in Chapter 4. The results are not as we initially expected, that the

depth of the profile would increase with the exposure time. On the other hand, the depth

seems not to correlate simply with time, while the fluorine concentration at the surface

does increase with time, and it is obviously in excess of the fluorine concentration in the

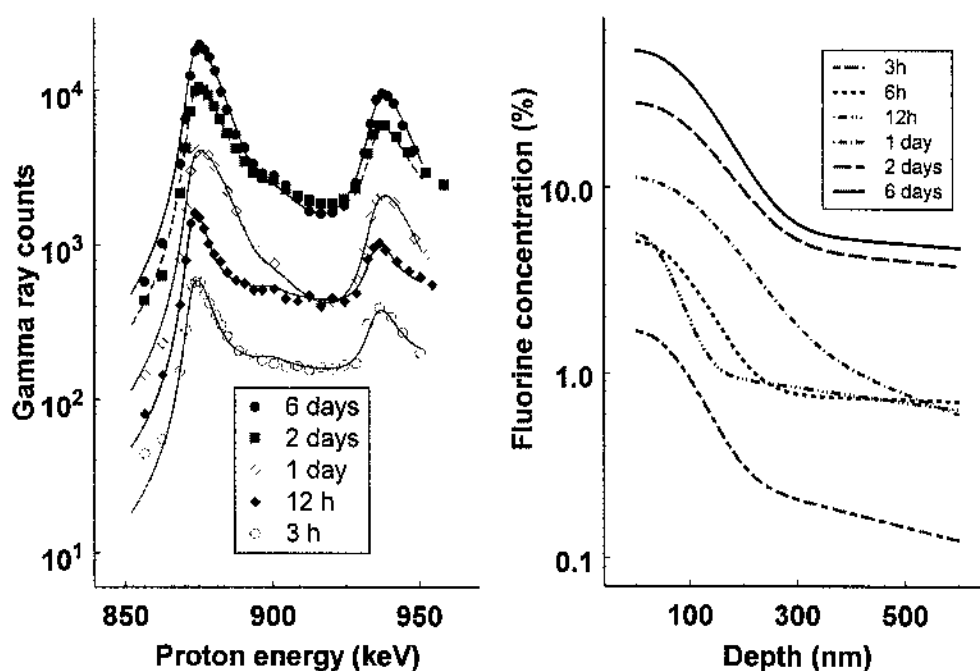solution after a short exposure time.

Fig. 5.2, NRA measurement of fluorine depth profiles in flint samples immersed for different times in an 80 °C 300 ppm NaF solution. At left are the experimental data points and their convolution fittings; at right are the fitting results.

This unexpected result suggests that fluorine surface adsorption is a rather slow process, and it continuously affects the diffusion profile, if we consider the uptake of fluorine into the flint "bulk" as the combination of surface adsorption and inward diffusion processes. As proposed in chapter 1, the fluorine uptake phenomenon is best conceived as the combination of the following processes: (i) Fluorine adsorption on the flint surface; (ii) Fluorine ion diffusion along the void network in the liquid phase and final adsorption by the surface (wall) of the voids; (iii) Diffusion of adsorbed fluorine ions along the surface of the grains, or so called grain boundary diffusion; (iv) Diffusion of adsorbed fluorine into the bulk, or so called solid state diffusion; (v) Dissolution of surface species.

All these five processes may contribute to the development of fluorine uptake profiles. However, surface adsorption seems to play the controlling role because the depth of fluorine uptake is not simply related to the time of exposure in accelerated aging, while the concentration continuously increases with the time.

5.3 Surface Adsorption

Surface adsorption seems to be very important in determining fluorine uptake profiles. Fluorine surface adsorption in flint from aqueous solutions with various fluorine concentrations and pH values has been investigated. The amount of adsorption is determined by integration of the near surface peak of the measured fluorine profile. Surface adsorption seems strongly influenced by the fluorine concentration and pH value in the solutions. Fig. 5.3 shows the amount of adsorption versus time for adsorption in a

fluoride solution with a NaF concentration of 100 ppm, and pH values of 4, 7, and 10

respectively. The lines are the best fit of the experimental data with the Elovich equation
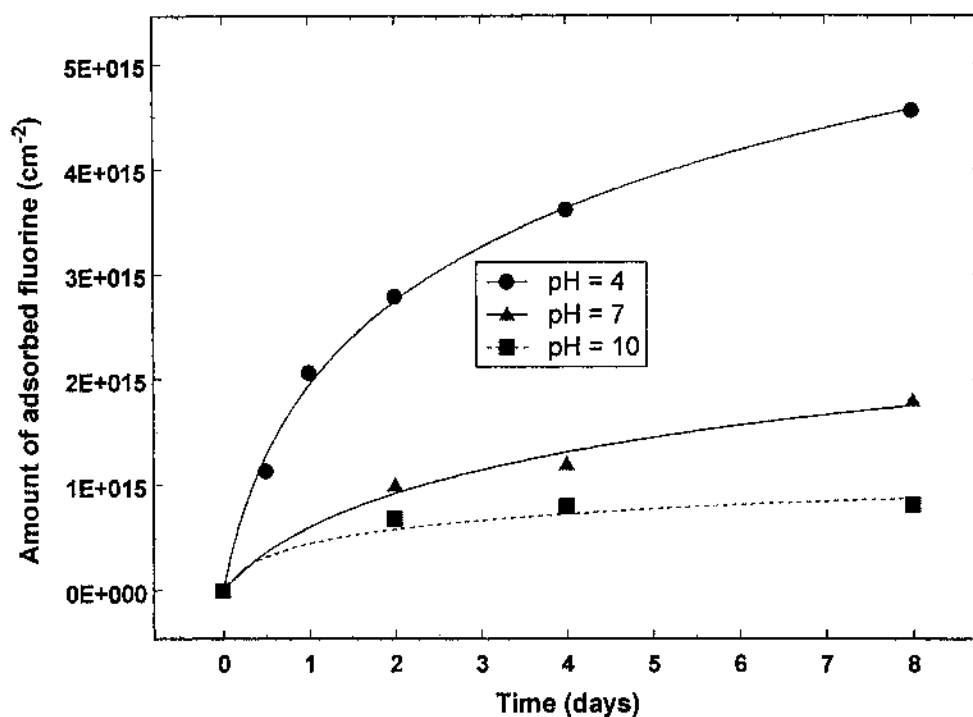
[HA64, HI81]:

Fig. 5.3, The variation of amount of fluorine adsorption in the near surface region with time for samples immersed in different pH values of the NaF solution with the same NaF concentration (100 ppm) at 80 °C.

$$q(t) = b^{-1} \ln(1 + t / k).$$ (5.1)

This equation is the solution to the differential equation

$$\frac{dq}{dt} = a \exp(-bq),$$ (5.2)

a relationship that appears in the general description of chemisorption kinetics at gas-solid interfaces. While differences are expected to exist between the fundamental mechanisms of gas phase chemisorption and the incorporation of fluorine ions into the matrix of the mineral, any process that follows a rate equation given by equations (5.2) will obey the Elovich equation. For example, the behavior of oxide formation in metal as well as in semiconductors has been confirmed to follow the same model [RI69, MA85].

Without detailed knowledge of the reaction one can nevertheless identify heuristically the significance of the fitting parameters. a is the initial (t=0) rate of adsorption, while the rate of growth approaches asymptotically $(bt)^{-1}$; b is a constant relating to activation energy for adsorption, and $k = (ab)^{-1}$.

One can observe in Figure 5.3 that fluorine surface adsorption is very dependent on the pH value of the solution. There is much more fluorine adsorption for the acidic conditions (pH=4) than for neutral (pH=7) or basic (pH=10) solutions. These results are consistent with the general behavior of anion adsorption in the solid-aqueous interfaces [HI81, ST80, SP84]. In general, the solid-aqueous interface is charged due to the imbalance of H^+ and OH^- bonded on the solid surface. The point of zero charge (pzc) is usually used to describe the characteristic of the surface charge. Lower pH value or higher H^+ concentration in the acidic solution increases the positive charge in the

interface, and therefore increases the surface adsorption of anions such as F⁻ from the

solution. On the other hand, a basic solution increases the negativity of the interface,

therefore decreasing the adsorption of F⁻. The pzc of a silica-aqueous interface is

between a pH of 2 to 3 [KI81, JA72, OS96]; therefore a silica surface is usually

negatively charged in a neutral solution or even a less acidic solution (pH > 2 to 3), and

hence does not easily adsorb fluorine ions.

Fig.5.4 shows how fluorine surface adsorption varies with time in fluoride

solutions with a pH of 7, and NaF concentrations of 30 ppm, 100 ppm and 300 ppm. The
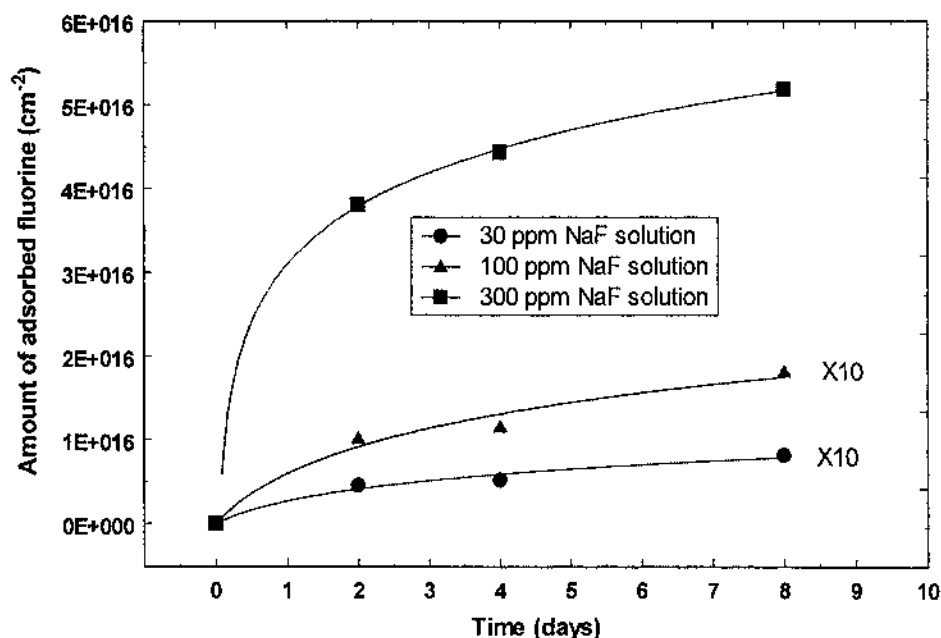

Fig. 5.4, The variation of the amount of fluorine adsorption in the near surface region with time for samples immersed in different concentrations of NaF solution with pH=7 buffer solution at 80 °C. The vertical scale for 30 ppm and 100 ppm plots is amplified 10 times.

experimental data are also fitted with the Elovich equation. The figure shows that

fluorine adsorption in the 300 ppm NaF solution appears to be dramatically higher than

that in the 100 ppm or 30 ppm NaF solutions. It also appears to follow Elovich kinetics

much better than in the other solutions. This result may suggest a concentration-

enhanced fluorine adsorption. However, the mechanism or chemical reaction that leads

to the enhanced adsorption is subject to further study.

5.4 Calcium Enhanced Adsorption

In the course of the investigation it was observed that samples of flint processed

in apparently the same manner might yield different fluorine uptake values. In particular,

extremely large differences of fluorine adsorption were observed in the NaF solution with

a pH value of 10 and a large amount of buffer solution. (In this particular experiment, the

100 ppm NaF solution with 50% of a pH=10 buffer solution was used, while it was the

standard practice to use 75% of distilled water and 25% of the buffer solution in all the

other experiments). XRF measurements showed that the fluorine surface concentrations

were strongly correlated with the calcium (Ca) impurities in the samples, as shown in Fig.

5.5.

This led to the following experiment to clarify the calcium-enhanced fluorine

adsorption. Three solutions were prepared: to one of them was added 0.05 wt% $CaCl_2$, to

another 0.5 wt% $CaCl_2$, and a third was kept $CaCl_2$ free; all of them contained 100 ppm

NaF and 10% of a pH=10 buffer solution. Flint samples were then immersed into these

solutions for fluorine uptake. The samples had also been measured using XRF for Ca

impurities before immersion into the solution. The Ca impurity levels in these samples were similar and on the order of 0.02 wt%. It was found that fluorine adsorption was greatly enhanced in the solution with $CaCl_2$, as shown in Fig. 5.6. Unlike the continuous adsorption in the solution without $CaCl_2$, the adsorption seems to reach equilibrium before 12 hours in the solution with the $CaCl_2$. The enhancements by the solutions with 0.5 wt% and 0.05 wt% $CaCl_2$ were comparable.
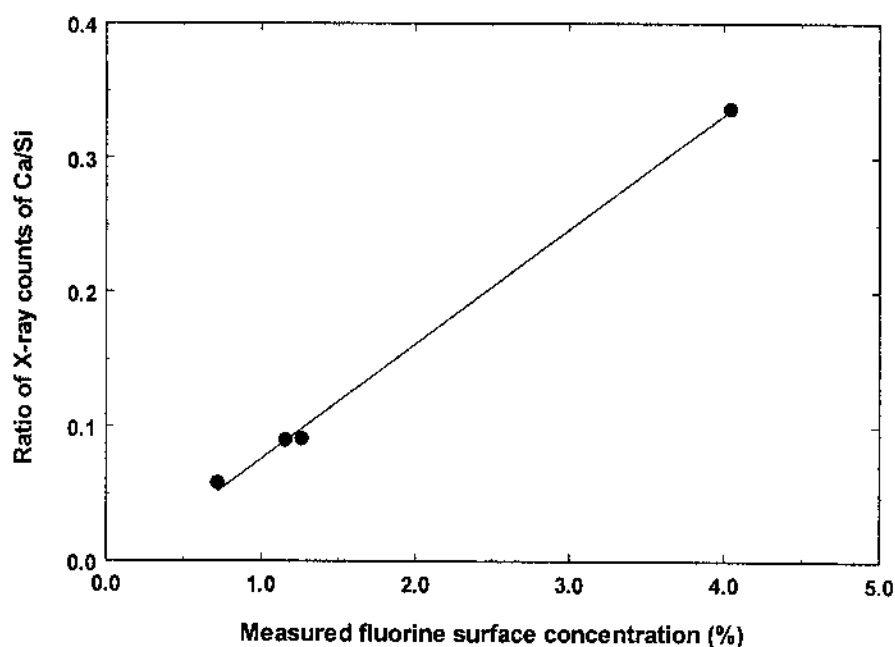

Fig. 5.5, Correlation of calcium impurity with fluorine adsorption in 4 different samples immersed in a 100 ppm NaF solution of pH=10 at 80 °C for 8 days.

Polycrystalline quartz samples were also used to study this calcium-enhanced fluorine adsorption phenomenon. Fig.5.7 gives the fluorine adsorption profiles of

polycrystalline quartz samples in a NaF solution with and without CaCl₂, along with a

flint sample in the solution with CaCl₂. One observes that fluorine adsorption is

enhanced by a factor of at least 100 in polycrystalline quartz samples. It also seems that

Ca-enhanced fluorine adsorption is much stronger in quartz surfaces than in flint

surfaces. This result further confirms that calcium in the solution strongly enhances

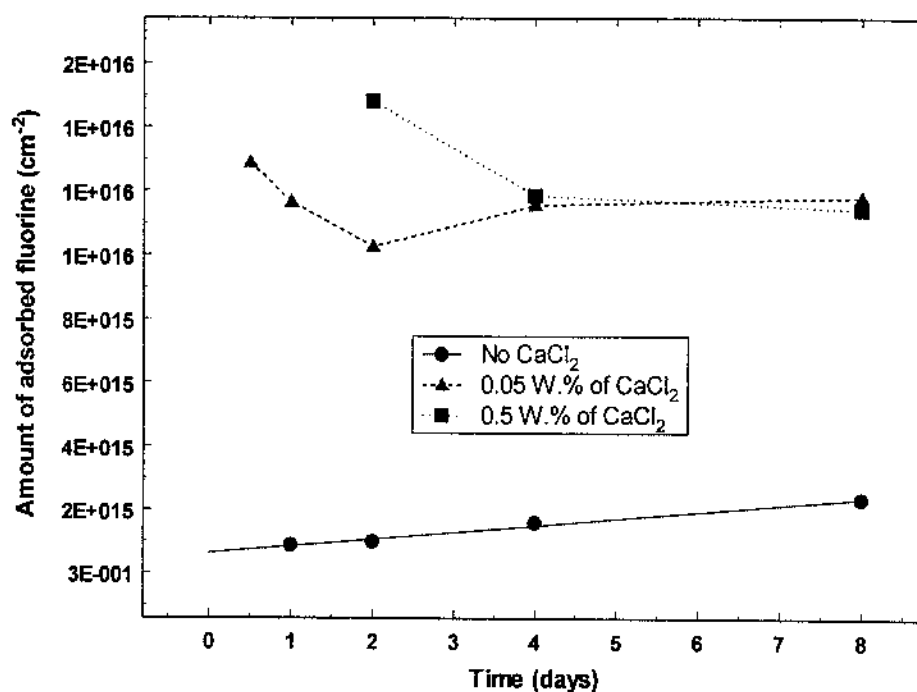fluorine adsorption in the silica surface in basic solutions.

Fig.5.6, The variation of fluorine adsorption in the near surface region with time of
samples immersed in 100 ppm NaF solutions with pH=10 buffer and with or without
CaCl₂ added to the solution.
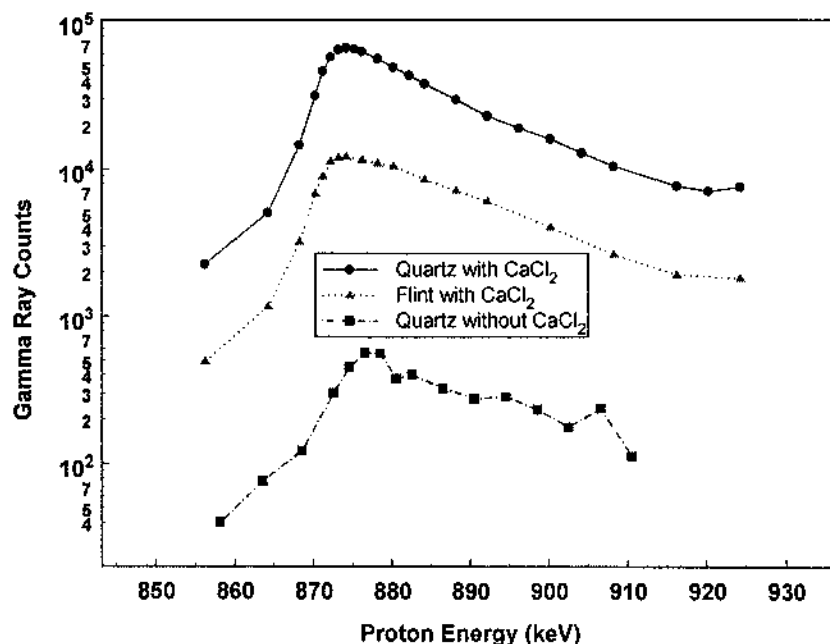
Fig. 5.7, Comparison of fluorine profiles of Quartz and flint samples in pH=10, 100 ppm NaF solutions with and without $CaCl_2$. Fluorine adsorption in quartz is enhanced by $CaCl_2$ by a factor of at least 100.

It is reasonable to hypothesize that the mechanism of calcium-enhanced fluorine adsorption is similar to that for Mg^{2+} enhanced adsorption reported by Rude and Aller [RU93]. The presence of Ca^{2+} may help to form a compound ion CaF^+ in the fluoride solution:

$$F^- + Ca^{2+} \leftrightarrow CaF^+.$$
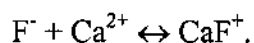
The negatively charged silica surface under basic conditions (pH =10) then would attract CaF^+ to the surface, and possibly, co-adsorb a F^- ion to form a stable CaF_2 molecule.

It was observed that when the CaCl$_2$ was added to the solution, a white solid was precipitated, because either Ca(OH)$_2$ or CaF$_2$ is not soluble in water. The solution with 0.5 wt% CaCl$_2$ precipitated more powder than the solution with 0.05 wt% of CaCl$_2$. Therefore, the Ca^{2+} levels in two solutions are controlled by the solubility of Ca(OH)$_2$ or CaF$_2$ in water, and should be at the comparable levels. This may explain why no significant difference of fluorine adsorption by these two solutions has been observed.

5.5. Temperature Dependent Study

Temperature is a very important parameter in almost any chemical phenomenon. Variation of fluorine adsorption with temperature was also studied in this dissertation. Fig.5.8 shows the amount of surface fluorine adsorption at different times for temperatures at 50°C, 60°C, 70°C, 80C°, and 100C°. The lines are drawn to guide the eye. The results seem to be quite messy partially because other parameters such as impurity levels and microstructure in the different samples are difficult to control. Nevertheless, one observes the following two general behaviors in Fig. 5.8:

(i) Fluorine adsorption seems to be high at medium temperatures (60°C, 70°C, 80°C), and low at low temperatures (50°C) and high temperatures (100°C).

(ii) At low temperatures, fluorine adsorption seems to be slow at the beginning (50°C, 60°C, and may increase continuously to a high level (60°C). At high temperatures, fluorine adsorption may reach equilibrium faster, and may even decrease with the time (100°C).
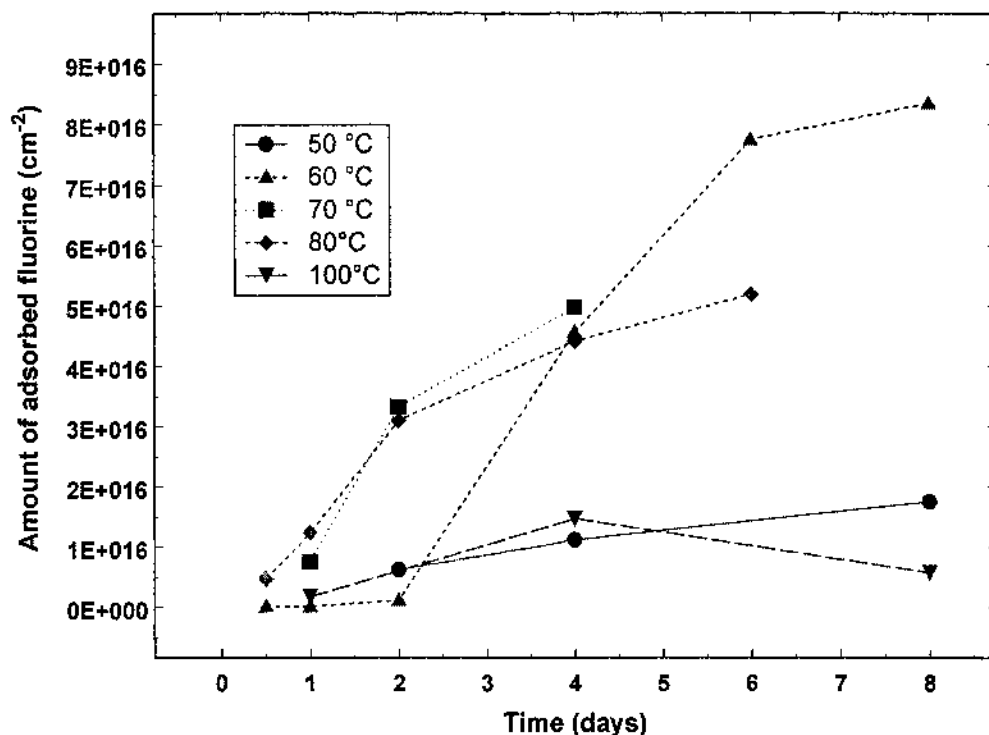
Fig. 5.8, Variation of fluorine adsorption in flint with time at different temperatures. The lines are drawn to guide the eyes.

A reasonable explanation of this result is that there is more than one chemical reaction in this phenomenon, especially the desorption and dissolution processes may be involved in the phenomenon.

5.6 Silica Etching and Dissolution

The etching or dissolution of SiO_2 by NaF solutions was studied using the ERD method. Samples of Si wafers with 254 Å or 800 Å of the SiO_2 film on the surface were

immersed in different NaF solutions for different times, and then measured for the thickness of the SiO_2 film using ERD. Fig. 5.9 shows the results. The left figure displays the etching (or dissolution) rates of silica by the NaF solution in different NaF concentrations when the solution is neutral (pH=7). The right figure gives the comparison of the etching (or dissolution) rate in different pH values while the NaF concentrations are the same (100 ppm, except for pH=7, 30 ppm and 300 ppm results also displayed). In both cases the solutions are kept at 80°C.

One observes that the rate of silica removal for different NaF concentrations at a neutral solution (pH=7) are almost identical. This result suggests that the removal of silica in a neutral solution is due to silica dissolution in the water, rather than some etching mechanisms associated with F^- ions, because the etching rate of silica by acidic fluoride solution is very correlated to the F^- concentration [CH97, JU71, OS96]. The dissolution rate appears to be very slow (about 7Å/day) in the neutral solutions.

It is also observed that the rate of silica removal is very dependent on the pH values of the NaF solution. The highest speed of silica removal is in the acidic solution, which is reasonably considered to be caused by an etching mechanism associated with HF [JU71, OS96]. The rate of silica removal in the basic solution is shown to be higher than that in the neutral solution but lower than that in the acidic solution. It is believed that the mechanism of removing silica in a basic solution is due to silica dissolution in the aqueous solution. Dove et al. has reviewed silica dissolution phenomena in NaCl and other aqueous solutions [DO94]. His own work and other earlier studies reveal that silica dissolution in aqueous solutions has a minimal dissolution rate at its pzc point (pH=2),

the dissolution rate increases as pH value increases [LI87, BE91, DO94]. The results in

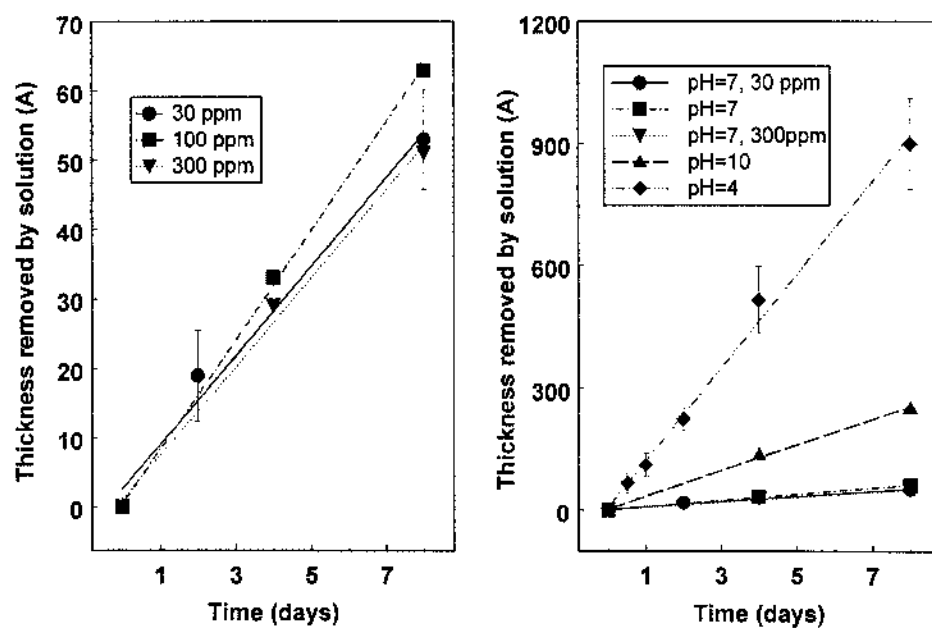this dissertation are consistent with Dove's conclusion.

Fig. 5.9, Silica removal rates by the NaF solutions at different concentrations and pH values.

CHAPTER 6

SUMMARY AND CONCLUSIONS

This dissertation has been focused on the study of the fluorine uptake phenomenon by flint mineral in aqueous fluoride solutions. Both theoretical and experimental approaches have been carried out. In a theoretical approach, a pipe diffusion model was used to simulate the complicated fluorine transportation problem, in which several diffusion mechanisms may be involved. An average concentration distribution function, which is dependent on the ratio of diffusion coefficients of the different diffusion mechanisms, and on the microstructure of the diffusion medium, was developed based on the pipe diffusion model.

In the experimental approach, the complicated fluorine uptake phenomenon has been investigated in several distinct aspects. The microstructure and material characterization of the flint samples, which play very important roles in fluorine uptake, have been studied using SEM, TEM, XRF, and other experimental methods such as weighing, dehydration and so on. The results suggest that Alibates flint, the material used in this study, has similar material characteristics to other flint minerals reported in the literature. Its typical microstructure is characterized as granular micro-quartz cemented with amorphous silica, which has a porous or void structure containing water. There are small amounts of impurities (below the level of 0.1wt%) such as Fe, Ca, and Ge in the material.

Several ion beam analysis methods have been developed to study the fluorine uptake problem. The NRA experimental method using the $^{19}F(p, \alpha\gamma)^{16}O$ reaction was used to measure the depth profile of fluorine in the material. Special problems in the experiment such as surface charging were studied. A computer data reduction program using a convolution fitting and deconvolution was developed. This program takes into account the effects of resonance width, the energy straggling and stopping power of protons in the material, and the interference of γ-rays from adjacent resonances. Another NRA method using the $^{1}H(^{19}F, \alpha\gamma)^{16}O$ reaction was also developed to measure hydrogen depth profiles. An ERD method was employed to measure the thickness of the SiO_2 film on a Si wafer, which was used to monitor the etching of silica by the fluoride solution.

The comprehensive study of fluorine uptake with various experimental conditions suggests that fluorine uptake is not a simple phenomenon, but rather the combination of several simultaneous processes including surface adsorption and inward diffusion. Surface adsorption seems to play the most important role in developing the fluorine uptake profiles in flint. The surface adsorption is affected by several parameters such as pH value, fluorine ion concentration, presence of Ca^{2+}, temperature, dissolution and desorption in the solution.

The results reveal that surface adsorption increases as the solution becomes more acidic (low pH value), which is consistent with the general rule of anion adsorption in a charged solid-aqueous interface. Surface adsorption also increases as fluorine concentration in the solution increases. However, the relation is not linear. Higher fluorine concentrations in the solution may dramatically increase fluorine surface

adsorption, suggesting that a fluorine-enhanced surface reaction may be involved in the adsorption. It was also found that the presence of Ca^{2+} in the solution strongly enhances fluorine adsorption in the silica surface, suggesting that impurities in flint may play important roles in fluorine uptake. The temperature dependent study reveals that fluorine surface adsorption does not simply increase or decrease as temperature increases, suggesting that fluorine surface adsorption is not a single thermally activated reaction. It was also observed that there is insignificant silica dissolution in the neutral fluoride solutions, while dissolution increases in a basic solution, and the silica is strongly etched in an acidic solution.

REFERENCES

[AD97] A.W.Adamson and A.P.Gast, *Physical Chemistry of Surfaces*, (John Wiley & Sons, Inc., New York, 1997), Chapter 5, 7, 11.

[BA77] C.A.Barnes, J.C.Overley, Z.E.Switkowski, and T.A.Tombrello, *Appl. Phys. Lett.*, **31**, (1977) 239.

[BA95] J.C.Barbour, B.L.Doyle, *Handbook of Modern Ion Beam Materials analysis*, Editors: J.R.Tesmer, M.Nastasi, (Material Research Society publication, 1995), Chapter 5.

[BE91] P.C.Bennett, *Geochim Cosmochim Acta*, **55** (1991)1781.

[BL81] W.E.Blass, G.W.Halsey, *Deconvolution of Absorption Spectra* (Academic Press, New York, 1981).

[BO82] F.Bodart, G.Deconninck, *Nucl. Instrum. and Meth.* **197**, (1982) 59.

[BO88] R.J. Borg & G.J.Dienes, *An Introduction to Solid State Diffusion*, (Academic Press Inc., San Diego, CA 92101, 1988).

[BR38] S.Brunauer, P.H.Emmett, and E.Teller, *J.Am.Chem.Soc.* **60**, (1938) 309.

[CH81] J.Chaumont, F.Lalu, M. Salome, A.M.Lamoise and H.Bernas, *Nucl. Instrum. and Meth.* **189**, (1981) 193.

[CH96] Yong-Chae Chung and Bernhardt J. Wuensch, *J. Appl. Phys.*, **79**, (1996) 8323.

[CH97] O.M.R.Chyan, J.Wu, J.-J. Chen, *Appl. Spectroscopy*, **51**, (1997)1905.

[CL63] Le Claire, *Brit. J. Appl. Phys.*, **14**, (1963) 351.

[CL78] G.J.Clark, CW.White, D.D.Allred, B.R.Appleton, F.B.Koch, C.W.Magee, *Nucl. Instrum. and Meth.*, **149**, (1978) 9.

[CO93] J.H.Conway and N.J.A.Sloane, *Sphere Packings, Lattices and Groups*, (2nd edition, Springer-Verlag, NY, 1993).

[DA95] S.Darta, *Ph.D Dissertation*, (Rochester University, 1995)

[DAV95] J.A.Davies, W.N.Lennard and I.V.Mitchell, *Handbook of Modern Ion Beam Materials analysis*, Editors: J.R.Tesmer, M.Nastasi, (Material Research Society publication, 1995), chapter 12, 343.

[DE83] G.Deconninck, B.Van Oystaeyen, *Nucl. Instrum. and Meth.* **218**, (1983) 165.

[DO79] B.L.Doyle and P.S. Peercy, *Appl. Phys. Lett.* **34** (1979)811.

[DO90] P.M.Dove, D.A.Crerar, *Geochim Cosmochim Acta* **54**, (1990)955.

[DO94] P.M.Dove, J.D.Rimstidt , *Silica: Physical behavior, Geochemistry and Materials Application*, Review in Mineralogy, Volume 29, Editors: P.J.Heaney, C.T.Prewitt, and G.V.Gibbs.(Mineralogical Society of America, 1994), Chapter 8.

[EC76] J.L'Ecuyer et al, *J. Appl. Phys.* **47** (1976) 881.

[EV96] J. W. Evans, *J. Appl. Phys.*, **82**, (1997) 628.

[FI50] J.C. Fisher, *J. Appl. Phys.*, **22**, (1950) 74.

[GE70] C.F.Gerald, *Applied Numerical Analysis*, (Addison-Wesley Publishing Company, Inc., Reading, Massachusetts, 1970).

[GR94] H. Graetsch, *Silica: Physical behavior, Geochemistry and Materials Application*, *Review in Mineralogy*, Volume 29, Editors: P.J.Heaney, C.T.Prewitt, and G.V.Gibbs. (Mineralogical Society of America, 1994) Chapter 6.

[HA64] D.O.Hayward, and B.M.W.Trapnell. *Chemisorption* (London: Butterworth's, 1964), 93.

[HI81] F.J.Higston, *Adsorption of Inorganics at Solid-Liquid Interfaces*, Editors: M.A.Anderson, and A.J.Rubin, (Ann Arbor Science Publishers, Inc., 1981) Chapter 2, p51.

[JA72] P.O.James, T.W.Healy. *J. Colloid Interface Sci.* **40**, (1972) 53-64.

[JA81] R.O.James, *Adsorption of Inorganics at Solid-Liquid Interfaces*, Editors: M.A.Anderson, and A.J.Rubin, (Ann Arbor Science Publishers, Inc., 1981) Chapter 6, p219.

[JA95] Jandel Scientific Software, *PeakFit User's Manuel* (Jandel Scientific Software, 1995).

[JE57] A.T.Jensen, C.J.Wohlk, K.Drenck and E.K.Andersen, Dan. *Nat.Inst.Build.Res.,*
Acad. Tech. Sci. (Progress Report DI, Copenhagen, 1957).

[JE92] S.P.Jeng, T.P.Ma, R.Canteri, M.Anderle, and G.W.Rubloff, *Appl. Phys. Lett.* **61**,
(1992) 1310.

[JE97] G.Jerkiewicz, *Solid-Liquid Electrochemical Interfaces*, ACS Symposium Series
656, (American Chemical Society, Washington, DC 1997) **Chapter 1.**

[JI97a] J. Jin, D.L.Weathers, J.P.Biscar, B.F.Hughes, J.L.Duggan, F.D.McDaniel, and
S.Matteson, *AIP conference proceedings 392*, (AIP press, New York,1997) 681.

[JI97b] J. Jin, and S.Matteson, *Numerical Study of Diffusion in Polycrystalline Materials*,
talk in APS Texas, 97 fall, Denton, Texas.

[JU71] J.S.Judge, *J. Electrochem. Soc.,* **118**, (1971) 1772.

[KA89] I. Kaur and W. Gust, *Fundamentals of Grain and Interphase Boundary Diffusion*
2nd ed. (Ziegler, Stuttgart, 1989).

[KA90] J. Kato, *J. Electrochem. Soc.,* **137**, (1990) 1918.

[KI81] D.G.Kinniburgh, and M.L.Jackson, *Adsorption of Inorganics at Solid-Liquid
Interfaces*, Editors: M.A.Anderson, and A.J.Rubin, (Ann Arbor Science
Publishers, Inc., 1981) Chapter 3.

[LA18] I.Langmuir, *J. Am. Chem. Soc.* **40**, (1918) 1361.

[LI87] D.T.Liang and D.W.Readey, *J. Am.Ceram. Soc.,* **70**, (1987) 570.

[MA77] J.W.Mayer, E.Rimini, *Ion Beam Handbook for Material Analysis*, (Academic
Press, Inc., New York ,1977).

[MA82] B.Maurel, G.Amsel, J.P.Nadai, *Nucl. Instrum. and Meth.* **197**, (1982) 1.

[MA85] S.Matteson and R.A.Bowling, *Mat.Res.Soc.Symp. Proc.* **Vol.48**, (1985) 215.

[MA86] B.S.Massey, *Measures in Science and Engineering*, (Ellis Horwood Limited,
Chechester, UK, 1986) Chapter 6.

[MA90] J.W.Mayer & S.S.Lau, *Electronic Materials Science*, (Macmillan Publishing
Company, New York, 1990).

[MA92] T.P.Ma, *J. Vac. Sci. Technol.* **A10**, (1992) 705.

[MO90] S.R.Morrison, *The Chemical Physics of Surface*, (Plenum Press, New York, 1990).

[NA00] National Park Service Bulletin.

[OR92] M.Orlowski, H.-H.Tseng, R.Hance, P.J.Tobin, *Workshop on Numerical Modeling of Processes and Devices for Integrated Circuits*: **NUPAD IV**, (IEEE, New York, 1992) 35.

[OS96] K. Osseo-Asare, *J. Electrochem. Soc.*, **143**, (1996) 1339.

[PO96] Ch. Poisson, A. Rolland, J. Bernardini, and N.A. Stolwijk, *J. Appl. Phys.*, **80**, (1996) 6179.

[RE92] Jens G. Reich, *C Curve Fitting and Modeling for Scientists and Engineers* (McGraw-Hill, New York, 1992).

[RI69] I.M.Ritchie and G.L.Hunt, *Surface Sci.*, **Vol.15**, (1969) 524.

[RO97] Roger Nix, *An Introduction to Surface Chemistry*, (WWW publication, address: http://alpha.qmw.ac.uk/~ugca000/surfaces/scc/) Chapter 1, 2, 3.

[RU93] P.D.Rude and R.C.Aller. *American J. of Science*, **Vol. 293,** (1993) 1-24.

[SE53] E. Segre, *Experimental Nuclear Physics* (John Willy & Sons, New York, 1953).

[SH72] W.Shepherd, *Flint, Its Origin, Properties and Uses*, (Faber and Faber, London, 1972).

[SP84] G.Sposito, *The Surface Chemistry of Soils*, (New York, Orford, 1984).

[ST80] W. Stumm, R.Kummert, L.Sigg. *Croatica Chemica Acta*, **53**, (1980) 291.

[SU64] T. Suzuoka, *J. Phys. Soc. Japan.*, **19**, (1964) 839.

[SZ94] Sc. Szeles et al, *J. Appl. Phys.*, **76**, (1994) 3403.

[TA75] R.E.Taylor, *World Archeology* **1**, (1975) 125.

[TS79] M.Y.Tsai, D.S.Day, B.G. Streetman, P.Williams, and C.A.Evans, Jr., *J. Appl. Phys.*, **50**, (1979) 188.

[VO83] R.D.Vold & M.J.Vold, *Colloid and Interface Chemistry*, (Addison-Wesley Publishing Company, Inc., Reading, Massachusetts, 1983).

[VU95] H.-H.Vuong, H,-J.Gossmann et al, *J. Appl. Phys.* **77**, (1995) 3055.

[WA90] P.Walter, M.Menu, I.C.Vickridge, *Nucl. Instrum. And Methods*, **B45**, (1990) 119.

[WA92] P.Walter, M.Menu, J.-C. Dran, *Nucl. Instrum. And Methods*, **B64**, (1992) 494.

[WA93] J.B.Wachtman, Z.H.Kalman, *Characterization of Materials*, (Butterworth-Heinemann, Stoneham, MA, 1993) 404.

[WE70] R.C. Weast (Editor), *Handbook of Chemistry and Physics*, 50th edition, (The Chemical Rubber Co., Cleveland, Ohio, 1970).

[WH54] R.T.P.Whipple, *Phil. Mag.*, **45**, (1954) 1225.

[WH61] J.F.White and J.F.Corwin, *Amer. Mineral.*, **46**, (1961) 112.